

ABSTRACT

Title of Thesis: EFFECTS OF TEMPERATURE AND AEROSOL
 CONTENT ON LASER-INDUCED BREAKDOWN
 SPECTROSCOPY DETECTION LIMITS

Kyle F. Kratzsch, Master of Science, 2004

Thesis Directed By: Assistant Professor, Steven G. Buckley,
 Department of Mechanical Engineering

Research to analyze effects of ambient temperature and aerosol dispersity on Laser-Induced Breakdown Spectroscopy (LIBS) detection limits is presented in this study. The theoretical results are applicable to future gas turbine exhaust monitoring with LIBS. Modification of a traditional LIBS system provides a method for in situ sampling in a gas turbine exhaust stream. Data collection in a controlled laboratory environment was performed with a LIBS system modified with an intrusive sampling probe to study the effects of temperature and aerosol dispersity on the limits of detection for chromium (Cr), magnesium (Mg), manganese (Mn), and titanium (Ti) particulate. Results show that increasing the temperature of the aerosol flow decreases the elemental mass required for LIBS detection, thereby increasing system sensitivity. Similar gains in system sensitivity occur when samples are taken from monodisperse aerosol relative to polydisperse aerosol. The lowest detection limits of 117 fg Cr, 95 fg Mg, 106 fg Mn, and 841 fg Ti occur when sampling from monodisperse aerosol flow at room temperature conditions.

EFFECTS OF TEMPERATURE AND AEROSOL DISPERSITY ON LASER
INDUCED BREAKDOWN SPECTROSCOPY DETECTION LIMITS

By

Kyle F. Kratzsch

Thesis submitted to the Faculty of the Graduate School of the
University of Maryland, College Park in partial fulfillment
of the requirements for the degree of
Master of Science
2004

Advisory Committee:
Assistant Professor Steven G. Buckley, Chair
Professor Michael Zachariah
Associate Professor Ken Kiger

ACKNOWLEDGEMENTS

This research was conducted at the University of Maryland under SBIR contract in conjunction with Systems Planning and Analysis, Inc. I would like to thank the Air Force and MIPS for financial support of the project.

I would like to thank the many people who contributed to my understanding and growth during this project. Dr. Steve Buckley, my advisor, who guided the research and helped identify the goals of the work. I would like to thank the members of my committee Dr. Ken Kiger and Dr. Mike Zachariah for their assistance in completing the necessary requirements and for the use of laboratory equipment. I would like to thank Ashish Rai, Anand Prakash, Dibyendu Mukherjee, Travis Tempel, Gregg Lithgow, Eddy Chen, and Chris Baldwin for their invaluable insight during the project. Finally, I would like to thank Annie, who is always my best supporter.

TABLE OF CONTENTS

Acknowledgments.....	ii
Table of Contents.....	iii
List of Tables.....	iv
List of Figures.....	v
Chapter 1 Introduction.....	1
1.1 Background	1
1.2 Component Wear in Gas Turbine Engines	2
1.2.1 Airfoil Wear	2
1.2.2 Bearing Wear	3
1.3 Emissions Monitoring Techniques	5
1.4 Objectives	6
Chapter 2 Literature Review	9
2.1 Process of Laser Induced Breakdown Spectroscopy	9
2.2 Physics in the Plasma Environment	10
2.3 LIBS Experimental Parameters	11
2.4 Applications of LIBS	15
Chapter 3 Apparatus and Procedure.	21
3.1 LIBS Apparatus	21
3.2 Sampling Probe	24
3.3 Aerosol Generation	25
3.4 Flow Reactor	31
3.5 Experimental Procedure	33
Chapter 4 Experimental Results.....	37
4.1 Calibration	37
4.2 Aerosol Characterization	41
4.3 Temperature Comparison	44
4.4 Dispersion Comparison	57
4.5 Comparison of Detection Limits	62
4.6 Error Analysis	64
Chapter 5 Conclusions.....	66
5.1 Summary of Results	66
5.2 Contributions to LIBS	67
5.3 Future Work	67
Bibliography..	69
Appendix A Matlab Data Processing Code	72

LIST OF TABLES

Table 3.5.1 - Detector gate width and delay ranges tested for each element.....	34
Table 3.5.2 - Classifier settings and resulting monodisperse concentrations.....	36
Table 4.1.1 - The optimum detector gate width and delay times.....	40
Table 4.2.1 - Elemental quantities aiding in calculation of total mass concentration in polydisperse aerosol stream.....	43
Table 4.3.1 - Polydisperse mass detection limits with relevant data for each element.....	56
Table 4.4.1 - Monodisperse mass detection limits with relevant data for each element.....	62
Table 4.5.1 - Mass detection limits for each heavy metal element.....	63

LIST OF FIGURES

Figure 2.3.1 - Manganese peak at 403 nm with regions of interest for calculating P/B ratio.	12
Figure 2.5.1 - Particle size distribution from gas turbine exhaust collected on filter and taken with a SMPS by Johnson [29].	18
Figure 3.1.1 - Generic LIBS experimental apparatus.	20
Figure 3.2.1 A. - Probe end containing laser focusing/emission collection lens.	23
Figure 3.2.1 B. - Opposite probe end with five tubes for inlet and outlet cooling water, and one for nitrogen lens purge.	23
Figure 3.3.1 - TSI 3076 atomizer with syringe pump[32].	25
Figure 3.3.2 - TSI 3075/3076 atomizer assembly [32].	26
Figure 3.3.3 - Particle detection efficiency, NaCl particles in nitrogen at 1500 cm ³ /min inlet flow.	29
Figure 3.4.1 - Flow Reactor with detailed view of cross-shaped test section.	30
Figure 3.4.2 - Burner assembly for high temperature monodisperse aerosol testing.	32
Figure 4.1.1 - Chromium aerosol particles, laser power 30 mJ.	37
Figure 4.1.2 - Chromium aerosol particles, laser power 60 mJ.	38
Figure 4.1.3 - S/N ratio curves from Fig. 4.1.2 with error bars representing +/- 1 standard deviation.	39
Figure 4.2.1 - Particle size distribution of Cr, Mg, Ti, Mn.	42
Figure 4.3.1 - Spectral hits binned by S/N ratio magnitude, polydisperse Mn at 21°C.	45
Figure 4.3.2 - Spectral hits binned by S/N ratio magnitude, polydisperse Mn at 420°C.	46
Figure 4.3.3 - Comparison of S/N ratio occurrences for Mn at 267649 fg/cc.	46
Figure 4.3.4 - S/N ratio as a function of Mg polydisperse aerosol concentration taken at room temperature.	47
Figure 4.3.5 - S/N ratio as a function of Mg polydisperse aerosol concentration taken at approximately 420°C.	48
Figure 4.3.6 - Number of Mn hits per 500 single shot spectra taken at different analyte concentrations.	49
Figure 4.3.7 - Concentration averaged spectra showing Ti elemental peaks.	50
Figure 4.3.8 - Detailed view of 334-339 nm from Ti spectra in Figure 4.3.7.	51
Figure 4.4.1 - Spectral hits binned by S/N ratio magnitude, monodisperse Mn at 21°C.	54
Figure 4.4.2 - Spectral hits binned by S/N ratio magnitude, monodisperse Mn at 420°C.	55
Figure 4.4.3 - Number of Mg hits per 1000 single shot spectra at different analyte concentrations.	56
Figure 4.4.4 - Number of Mn hits per 1000 single shot spectra at different analyte concentrations.	57
Figure 4.4.5 - Concentration averaged spectra showing Mn elemental peak at 403 nm, T=21°C.	58

Figure 4.4.6 - Concentration averaged spectra showing Mn elemental peak at 403 nm, T=420°C.	59
Figure 4.4.7 - S/N ratio as a function of Mn monodisperse aerosol concentration taken at approximately 21°C.	60
Figure 4.4.8 - S/N ratio as a function of Mn monodisperse aerosol concentration taken at approximately 420°C.	61

CHAPTER 1 Introduction

1.1 Background

Combustion processes, whether occurring in internal combustion engines, large-scale power generation, or waste incineration, are ubiquitous in our daily lives. The benefits of energy-intensive processes do not come without a price, in particular the products formed from combustion processes that are subsequently released into the environment. Emissions may be hazardous to human health, pose varying levels of threat to the environment, or provide insight into the efficiency and chemistry of the combustion process. Laser Induced Breakdown Spectroscopy (LIBS) provides a real-time method of monitoring elemental concentrations in effluent waste streams from combustion reactions, or a variety of sampling environments. Increasingly stringent EPA regulations concerning gas turbine engines operating at high atmospheric elevations motivates the development of real-time, portable emissions monitoring systems for aircraft engines. The application of LIBS for in situ analysis of elemental wear debris in a gas turbine exhaust plume was the practical objective of this study. Engine health monitoring systems incorporating LIBS may provide unique opportunities in diagnosing potential mechanical failures. Preliminary investigation into the effects of ambient temperature and aerosol composition on LIBS detection capabilities comprised the fundamental research objectives. Quantifying and understanding those effects would lead to more appropriate usage of the LIBS technique.

The gas turbine is a complex machine consisting of three main components: the compressor, combustor, and turbines. The compressor pressurizes the ambient air flowing into the combustor, where fuel is injected and combustion generates high

pressure, high velocity gas. The turbine transfers the energy contained in this gas to mechanical work via the output shaft. The shafts and connected engine components attain significant rotational rates within an environment of extreme pressure and temperature, resulting in inevitable degradation of the aerodynamic engine components. Highly specialized materials and advanced mechanical construction of components are necessary to prolong the life of turbine components.

LIBS measurement systems have been deployed as real-time emissions monitors in diverse environments including high temperature boilers and furnaces [1], industrial exhaust streams [2], and incinerator waste streams [3]. The idea of using plasmas as an excitation source for atomic spectroscopy was first proposed in the mid-1960's [4]. A wide proliferation of LIBS techniques and applications has occurred in the past 25 years. LIBS is used mainly for qualitative spectroscopy, however, techniques can be incorporated to gain information describing the quantitative properties of the sample species.

1.2 Component Wear in Gas Turbines

1.2.1 Airfoil Wear

Degradation of gas turbine components results from many processes [5-6]. The airfoils, or individual blades in the turbine and compressor stages of the engines, are susceptible to fouling, oxidation, cracking, spalling, corrosion, erosion, and thermal stress. Fouling is the buildup of particles by adherence to airfoils and other surfaces. The result is increased surface roughness and changes in shape of the airfoils, or turbines. Oxidation can occur as oxygen from the surrounding high temperature gas reacts with

metal engine components. Oxidation of coatings and substrates leads to corrosion and increased susceptibility to mechanical wear such as cracking and spalling. Impact wear due to environmental debris and thermal loading fatigue also result in weakened components. Thermal fatigue influenced by the coatings and environment can cause defects in the airfoil and micro-structural features.

The degradation processes above dramatically change the surface characteristics of airfoils and other material components. This leads to changes in tolerances and ultimately decreases engine performance. It is accepted that monitoring the concentration of the particulate could provide insight into the condition of specific components. Knowing the elemental composition of the wear debris could lead to the identification of particular components undergoing significant wear.

1.2.2 Bearing Wear

The main shaft gas turbine bearings are additional important examples of engine components whose wear could lead to the presence of metal particulate in the engine exhaust. A failure of the bearings or the race containing the bearings can result in substantial damage to the entire engine. This motivates the need to monitor the condition of the main shaft bearings in an attempt to detect fatigue so that replacement can prevent failure. Many studies have been performed to determine the effects of various parameters on the fatigue life of bearings [7-9]. These parametric studies have analyzed various bearing rotational speeds, thrust loadings, types of stresses, bearing and lubricant temperatures, and cooling and lubricant flow rates, and worked to develop more accurate fatigue life theory.

The thrust-load carrying main shaft ball bearing is one of the most important components in an aircraft gas turbine [8]. There may be more than one such bearing depending on the design of the engine. Roller bearings are in place to provide further support of the main shaft and will carry applied radial loadings which may approach 1 g [8]. The thrust and roller bearings are required to carry these loads in extreme conditions of high rotational speed and high temperature; the shaft rotates at speeds of 10,000 rpm and higher, depending on the diameter, and temperatures frequently reach 200 to 250°C (400 to 500°F) [9]. The bearing components are typically fabricated from vacuum induction melted, vacuum arc remelted (VIMVAR) M50 tool steel that is through-hardened to withstand the extreme operating conditions. The metallurgical improvements made to this steel over the course of three decades allow the bearings to perform successfully under demanding conditions. When bearings fabricated of this steel do experience rolling contact fatigue, it occurs as spalling and flaking from the surfaces.

Significant analysis of the surface wear on bearings that had been taken from engines after varying periods of operation has been presented by Averbach et. al. [10]. Examination of these bearings showed substantial evidence that the wear that led to failure originated at the surface rather than at subsurface sites. There are multiple ways that initial damage could form on the bearing surfaces, including grinding grooves from finishing procedures, score marks from hard abrasive particles in lubrication, dents caused by non-abrasive particles, and corrosion pits. These incidents are typical of metal-to-metal contact that is present between the bearing and both the main shaft and the race. Once the initial damage was done, peeling could occur in the area surrounding the damaged surface. This area was plastically deformed and susceptible to peeling, which

would grow and develop into spalls. The surface damage indicates that bearing material is released due to the initial occurrence or in the form of peels or spalls. These debris particles ($<0.15\mu\text{m}$) leave the bearing race and exit the engine in the exhaust stream.

1.3 Emissions Monitoring Techniques

The recent trend in monitoring effluent waste streams involves continuous emissions monitors (CEMs). CEMs primarily function to gather data proving compliance with federal regulations, and more recently to satisfy public scrutiny of emissions. Another role of CEMs is to provide information about the process allowing performance enhancement and optimization. The latter role of CEMs is fundamental to this study of detecting increases in heavy metal-containing particulate in gas turbine exhaust in order to avoid catastrophic failure of the engine. The capabilities of two other candidate systems summarized briefly below provides a comparison with LIBS, which is the only system experimentally tested in this study. The alternative methods reviewed below are similar to LIBS in purpose and differ in plasma generation technique.

Inductively Coupled Plasma Atomic Emission Spectroscopy (ICP-AES) ignites a plasma with a plasma torch, which is an apparatus consisting of concentric tubes with the outermost tube surrounded by an induction coil. The inner tube is the injector and transports an aerosol carrier gas to the plasma sampling region. The intermediate tube carries auxiliary gas, while the outer tube carries the plasma gas that cools the tube assembly. Argon is typically used in plasma torches [11, 12]. The plasma ignition process begins by purging the torch with argon. Subsequently, a high frequency electrical field is then applied to the induction coil, building up an alternating magnetic

field. An igniting spark (high voltage or Tesla spark) produces charge carriers which accelerate and create the plasma region. The torch plasma requires a stabilizing time period before sampling can occur [12]. The advantages of ICP-AES include short analysis time, ability to sample particulate in the form of aerosol, the ability to sample multiple elements concurrently, a linear relationship between intensity and particulate concentration, and high sensitivity. The significant disadvantage for this study is the inability for in situ test sampling. The aerosol must be injected into the plasma through the torch, requiring it to be removed from the original environment.

Microwave Induced Plasma Atomic Emission Spectroscopy (MIP-AES) is similar in operation to the ICP technique, a plasma torch is used to create the plasma sampling volume and the aerosol carrier gas is fed into the torch through an inner axial tube injecting directly into plasma. MIP uses helium as the plasma support gas and preferably as the analysis carrier gas as well due to the absence of significant matrix effects. The matrix is the sum of all components of a sample, which may cause analytical errors referred to as matrix interference [12]. MIP consumes much less power in operation than ICP, and therefore creates a smaller plasma volume with lower excitation temperature and less sensitivity [13], but is similarly limited to analysis of extractively sampled, rather than in situ, aerosol.

1.4 Objectives

The following chapters describe a set of experiments designed to quantify the performance of a LIBS system integrated with an optical sampling probe to measure metal particulates of interest; specifically chromium (Cr), magnesium (Mg), manganese

(Mn), and titanium (Ti), in conditions involving elevated temperatures and varying aerosol content. LIBS has had limited application as a CEM [1, 2, 3, 14] technique and effects of temperature and aerosol content on detectability have previously not been examined. Characterization of these two parameters will provide insight into applying LIBS as a gas turbine CEM to measure wear debris particulate.

The system under study was developed and calibrated at the University of Maryland as a precursor to development of a mobile intrusive system for future on-site testing in actual engine exhaust for the Air Force. Along with the hardware development of a LIBS system to be used as a gas turbine health monitor, a detailed study of factors affecting LIBS performance were addressed during the laboratory testing. There have been studies into factors affecting LIBS performance [15, 16, 17] and plasma spark generation [18] but none have looked at ambient temperature and aerosol distribution affects on limits of detection (LOD). The following goals were a priority in the laboratory stage of testing:

- Quantify probe performance in sample intensity transmission.
- Construct an appropriate probe stand for on-site engine testing.
- Develop a robust, complete sampling system for on-site engine testing.
- Determine effects of ambient temperature on concentration LOD.
- Determine changes in LOD when aerosolized metal is characterized with polydisperse or monodisperse size distributions.

In summary, the driving objective behind this research was the development of a physical LIBS system to perform in situ sampling of metal particulate in gas turbine exhaust, which is a new application for the LIBS technique. While many studies have

addressed factors that investigate the performance of LIBS in terms of plasma generation or detectability limits, no previous work has been done to study the effect of temperature and aerosol characteristics on the concentration LOD. Testing the effects of temperature and aerosol characteristics has provided interesting results related to system performance.

Following construction and calibration, the on-site acceptance testing phase will begin. The system developed in the laboratory at the University of Maryland will be sent to a field location where testing in an actual gas turbine exhaust plume will occur. This will lead to a further phase of system calibration and performance optimization for field data collection. Along with government military interest, Pratt and Whitney has shown commercial interest in an engine health monitoring system of this nature.

CHAPTER 2 Literature Review

2.1 Process of Laser Induced Breakdown Spectroscopy

Interest in plasmas as an analytical sampling environment began in the early 1960's [4]. Since then, work has been done using a separate laser beam as a probe to measure plasma characteristics such as electron density spatial distribution, through interferometry [19]. Laser Induced Breakdown Spectroscopy (LIBS), also called Laser Induced Plasma Spectroscopy (LIPS), is a spectroscopic technique utilizing laser-generated plasmas as the source of emission spectrum for analytical purposes. The plasma is created using a high-powered laser beam focused to a small spot using a lens. As the laser beam narrows approaching the focal point, the energy density increases promoting multiphoton ionization and electron impact ionization. The medium becomes optically thick and most of the energy in the latter part of the laser pulse is absorbed. At very short times, the ensuing plasma is not in equilibrium, after $\sim 1 \mu\text{s}$, equilibrium is reached, and temperatures are in the range of 10,000-25,000 K [18]. The plasma initiates in a heated vapor region where absorption by electron-neutral inverse Bremsstrahlung begins. As more electrons are created, a transition of the dominant laser absorption mechanism to electron-ion inverse Bremsstrahlung occurs [19]. This plasma spark functions as the sampling volume for the spectroscopic analysis. The spark can be focused on a solid surface or in a liquid or gas phase system. The electromagnetic radiation leaving the spark is then collected through focusing optics and carried by an optical fiber to the spectrometer.

2.2 Physics in the Plasma Environment

The underlying physics of the laser-induced plasma is relevant to understanding the mechanisms behind LIBS atomic emission and the subsequent data collection. At the atomic level within plasma, Salzmann [20] describes three general areas of interest. First is the role of the plasma environment on the atomic/ionic potential. Second is the ion-ion and electron-ion collisions that change the charge and excited state distributions. Third, and most relevant to this study, is the atomic emission and absorption spectra generated by the plasma.

When the high temperature plasma is formed, thermal energy breaks molecular bonds and may ionize atoms. Additional energy may excite an outer shell electron of the atoms or ions into a higher orbital, which is referred to as an excited state. The electron falls back to the lower energy level as the atom cools, spontaneously emitting the energy it originally absorbed from the plasma. The intensity of emission, I_{em} , is given by

$$I_{em} = A_{ji} h \nu_{ji} [N g_i / g_0 \exp(-\Delta E / KT)], \quad (2.1)$$

where h is Planck's constant, ν is the frequency of the transition, and the term in brackets is the Maxwell-Boltzmann equation [21]. This emission of radiation is collected and sent to a spectrometer, which measures the intensity versus wavelength of the radiated light. The distribution of the spectral lines for a given element is not random and can be determined theoretically. Niels Bohr determined that every atom is allowed only certain discrete and characteristic energy values [22]. Since the emission of radiation is proportional to the difference between the excited and ground atomic energy states, there are a finite number of spectral terms for an element. Atomic spectral information is readily accessible on the NIST online spectral line database, <http://www.nist.gov>.

2.3 LIBS Experimental Parameters

Carranza and Hahn [23, 24] have performed experimental and analytical analyses of LIBS sampling statistics for aerosol particles and relevant spatial and temporal effects associated with the plasma. A unique characteristic of LIBS is the ability to collect either single-shot spectral data or accumulations of sample shots. In accumulation mode, the signal intensities are summed over a number of shots to form an ensemble average, which is typical in LIBS experimentation. Ensemble averaging enhances sensitivity and precision by overcoming shot-to-shot variation [23] as noise in a random system decreases with $n^{1/2}$ where n is the number of samples. For discrete sampling events such as aerosol particles in dilute flows, single-shot spectra provide insight into elemental composition and concentration in a single plasma spark volume at one instant in time. Therefore, individual particles can be measured. The statistical variations from shot-to-shot are significant and can be resolved both spatially and temporally. Typically the plasma sampling volume ($\sim 1 \text{ mm}^3$) is many orders of magnitude larger than the particulate being studied (in this study $< 1 \text{ }\mu\text{m}$) and knowledge of the significance of particle location within the plasma in relation to output signal intensity is limited. Furthermore, the choice of collecting the sample signal orthogonal to laser location versus collecting axially aligned with laser beam may further affect spatial resolution due to location of particle in the plasma [currently being studied by Lithgow et. al]. Temporal resolution is critical in optimization of the LIBS signal due to the role of plasma temperature in the emission process discussed above [15]. Optimizing gate width and delay for specific elements will maximize spectral signal intensity. Carranza and Hahn report thermal equilibrium in the plasma to be realized after $1 \text{ }\mu\text{s}$, providing a lower

limit on gate delay [23]. Both spatial and temporal resolution are important in maximizing the peak-to-base ratio (P/B), the ratio of the elemental atomic emission intensity to the continuum or background emission intensity [23]. The P/B ratio offers a simple measure with which to analyze spectra to determine whether an emission line represents a particle hit, and to quantify concentrations. The method of calculation is

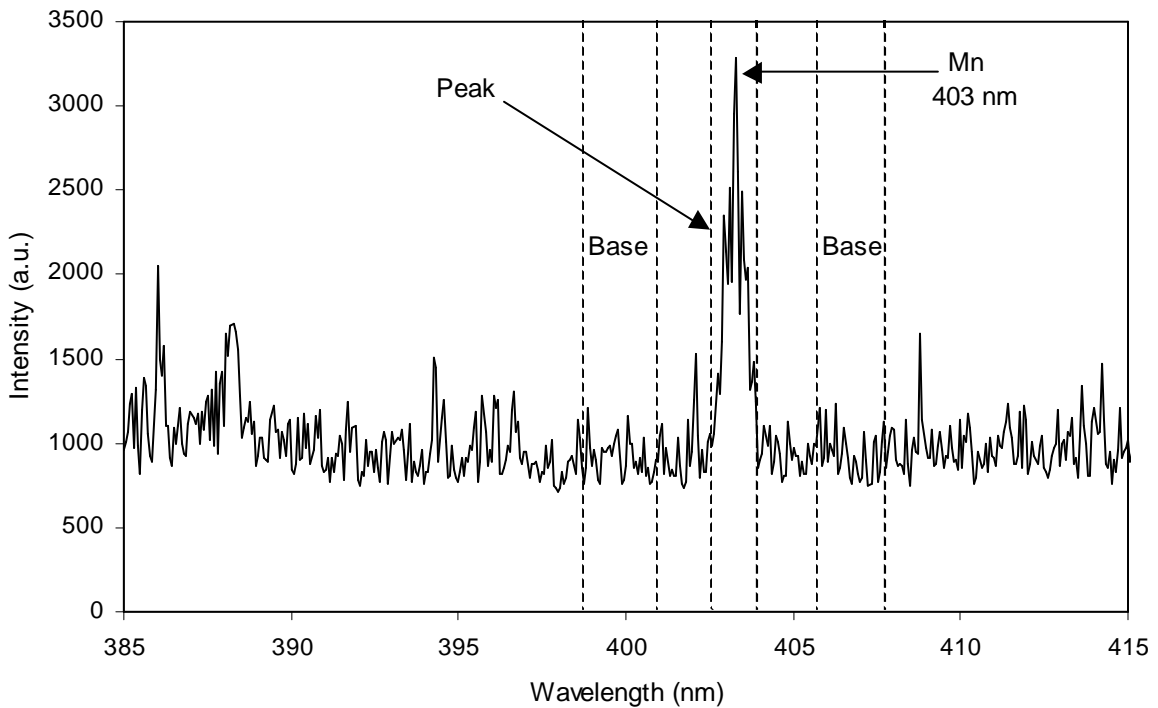


Figure 2.3.1 - Manganese peak at 403 nm with regions of interest for calculating P/B ratio.

discussed below in Figure 2.3.1. The P/B ratio is a ratio of integrated peak area to a projected baseline area. The peak area is calculated by integrating the signal intensity across the peak width, indicated in Figure 2.3.1 by the peak region. The baseline area is found by identifying one or more interference-free baseline regions on either side of the peak. The continuum emission that this represent is proportional to the "strength" of the plasma, and thus proportional to laser power. The ratio of the peak to the baseline region

thus largely removes the atomic emission dependence on laser power, eliminating fluctuations that might be caused by beam steering, particulate matter in the flow, laser power fluctuations, etc. The noise floor is calculated by determination of the root-mean-square fluctuation in the baseline, multiplying by the peak width to obtain a peak-equivalent noise, and then multiplying by a (standard) factor of three to determine the integral of the smallest peak that could be expected to be detected above the noise floor, P/B_{LD} , as defined in Equation 2.3. This calculation is used to determine the smallest measurable concentration from an ensemble of spectra; using a calibration for P/B versus concentration, P/B_{LD} determines the concentration corresponding to the limit of detection.

$$P / B = \frac{\int_a^b I_p}{\sum_i \int_{c_i}^{d_i} I_{b,i}}, \quad (2.2)$$

where I_p = Intensity values across the peak interval,
 $I_{b,i}$ = Intensity values across the background region i ,
 c_i, d_i = pixels denoting boundaries of background region i .

$$P / B_{LD} = \frac{3 \cdot \overline{RMS_{BG}} \cdot \sum_i |c_i - d_i|}{\sum_i \int_{c_i}^{d_i} I_{b,i}} \quad (2.3)$$

When performing single-shot LIBS analysis for the detection of individual aerosol particles, plasma volume plays a crucial role in particle hit rate. Increasing the plasma volume with respect to ambient environment increases the probability of particle hits. Plasma volume fluctuates slightly from shot-to-shot due to fluctuations inherent in laser energy output and variation in the breakdown process caused by the breakdown medium (air, solid, etc.). The plasma spark volume can be calculated using three different

methodologies described by Carranza and Hahn [24], but for the purposes of this work, a basic physical estimation of the laser generated plasma volume is appropriate. The volume was estimated based on a conical plasma volume, whose length was measured with a ruler mounted in line with the plasma spark. The plasma length coupled with angles determined from the lens focus length allowed for the calculation discussed in Chapter 4.

LIBS relies on robust plasma spark generation for temporally and spatially consistent sampling in ambient conditions. Yalcin et. al. [18] examined ambient effects on plasma properties for laser spark generation in air. Temperature and electron density within the spark were quantified to determine the effects of variation in ambient gas, the laser energy, particulate levels, and humidity levels. A Saha-Boltzmann analysis was developed to calculate spark temperature and a laser-supported radiation wave model of the plasma growth determined electron density. It was concluded that the ambient variables listed above had only a small influence on temperature and electron density in the spark at short times ($< 2 \mu\text{s}$) following breakdown.

LIBS measurement parameters must be adjusted for each element to optimize data collection precision. Fisher et. al. [15] explored the importance of temporal gating of the detector when optimizing signal collection. Six toxic metals were analyzed at eight different gate delays. Overall, emission generally decays with time as the plasma cools, so as the delay was increased, the width was also increased to compensate for lower emission. However, in many cases the continuum background (which contributes noise) decays much faster than the atomic emission, which has a temporal optimum based on the temperature of the plasma for a given line [23]. In the present research, two laser

power settings were included in the test matrix. Results showed 8 of the 9 elemental lines - of interest had longer optimal gate times when higher laser power was used to create the plasma. This coincides with the discussion above in Section 2.2, which explained that the rate of emission is a function of the plasma temperature, which is a function of time.

Castle et. al. [16] studied the influence of a broader set of system and environmental variables on the precision of LIBS measurements on solid samples. Their results were classified into two groups, consisting of variables affecting precision within a single set of measurements (intra-measurement) and precision between sets of measurements (inter-measurement). The data presented in the paper shows that the optimization of each occurs under different conditions. It was found that inter-measurement precision could be optimized by considering translation velocity of the solid sample, laser pulse energy, and number of spectra averaged. Intra-measurement precision benefited from considering translational velocity, pulse energy and gate delay. The percent change in random standard deviation in the data set was used to determine variable impact on the precision of the measurement.

2.4 Applications of LIBS

Radziemski [4] compiled a review of LIBS applications from 1987-1994 to document the versatility of the technique as an analytical tool and Lee et. al [25] composed a more recent review of LIBS applications; these works are excellent single-source references. A thorough analysis of more recent work in LIBS [1-3,14,26-30] provides a broad set of applicable fields of study. To the author's knowledge, no previous

work in applying LIBS to perform real-time in situ gas turbine exhaust analysis for metal particulate has been done.

LIBS has been used extensively as a waste stream CEM looking for both metal particulates and chemical species in exhaust. Buckley et. al. [3] used LIBS to monitor toxic metals present in exhaust from incinerators and a Department of Defense confined-burn facility. In this work, the conditional data analysis technique resulted in an overall detection limit of between 2 and 100 $\mu\text{g}/\text{dscm}$ (dry standard cubic meter) for toxic metals Be, Cd, Cr, Hg, and Pb. The conditional analysis consisted of filtering the spectra containing desired particle signals (hits) from spectra containing no relevant information (misses) by applying a minimum threshold criteria to the atomic emission. An average spectrum is then generated from an ensemble average of the shots determined to be hits. A sample probe was inserted in the effluent waste stream far from ductwork flow disturbances and the plasma spark was created directly in the wastestream.

Hahn et. al. addressed the statistical issues present when sampling in effluent waste streams with LIBS by developing Monte Carlo simulations for comparison with experiments [14]. The Monte Carlo simulations were used to address questions concerning the necessary number of particle samples required to represent accurately the true particle size distribution and the true sampling frequency. The simulations served as a comparison standard to the experimentally determined effluent concentration values. A conditional analysis approach was used where single-shot particle misses are filtered from single-shot particle hits to take advantage of discrete particle signals at potentially limiting particle sampling rate. Therefore, a higher S/N ratio can be attained while

maintaining concentration levels similar to those generated with Monte Carlo simulations.

There are methods in use to increase the hit rate in a data set of single-shot spectra [28]. Ottesen et. al. incorporate a particle detection system using light scattering to trigger the production of a plasma spark. A He-Ne laser is focused to a point in the path upstream of the plasma spark region. Particles that pass through the He-Ne laser focal point will scatter light which is detected by a photomultiplier tube. When the scattered light collected by the photomultiplier tube is above a given threshold value the Nd:YAG laser is triggered to produce a spark to hit the oncoming particle. The carrier gas velocity and distance between detection focal point and ablation focal point must be known to accurately determine Nd:YAG pulse timing.

Neuhauser et. al. [2] enlisted another LIBS technique in a system designed to monitor Cr levels in an electroplating facility waste stream. The aerosol stream was divided with 2.4 L/min guided to a filter sampling unit, with the remaining 0.6 L/min piped to a heated flow cell where the plasma spark would be generated. The flow cell was heated to prevent condensation on the quartz walls which can reduce or block signal transmission. The filter sample provided a calibration standard of comparison for the LIBS results. It was found that the instrument's dynamic range, response time, and the quantified detection limit of $14 \mu\text{g}/\text{m}^3$ of Cr were more than sufficient to meet German emission regulations.

Much of the research addressing the characterization of particulate in gas turbine exhaust has focused on the impact of particulate matter on the environment; specifically on the influence of particulate matter on the radiative properties of the atmosphere, anthropogenic climate change, and ozone depletion [27]. Johnson et. al. [29] used a scanning mobility particle sizer (SMPS) system to generate the particle size distribution in the Figure 2.5.1, below. A probe extracted engine exhaust from the plume which was

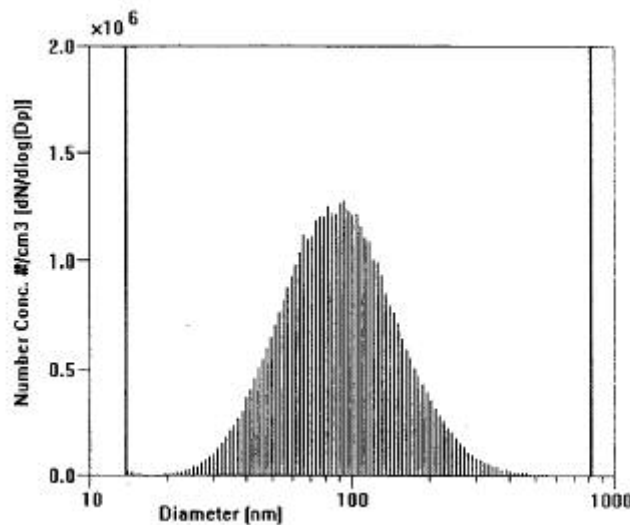


Figure 2.5.1 - Particle size distribution from gas turbine exhaust collected on filter and taken with a SMPS by Johnson [29].

transported to the SMPS via a heated line to reduce particle losses and condensation. From Fig. 2.5.1, the number mean particle diameter is approximately 90 nm and particles were in the range from 15-600 nm for the unspecified engine used for the collection. Simultaneously, soot samples were collected with a carbon substrate filter placed in the exhaust path and transmission electron microscopy allowed examination of structure and morphology of the soot.

Boyle's [31] study of heavy metal particulate emission focused on adverse affects on the environment and human health as well. Particulate was collected from two

engines burning JP-5 fuel at test facilities, by passing exhaust through filters, and additional particulate was collected at wetlands in proximity to airports, through soil samples. Analysis of the particulate collected from exhaust streams indicated zinc, copper, lead, beryllium, cobalt and vanadium. These heavy metals appear in the particulate in varying concentrations depending on thrust loading of the engine and correlate to fuel flow rates. Data presented shows particulate sizes smaller than 1.5 μm which agrees with that of Johnson [29].

Petzold et. al. [27] used an in situ probe placed in exhaust stream of a jet engine to sample exhaust and carry aerosol to a series of filters later analyzed for mass concentration and composition of carbonaceous particles. The study focused on carbon black and the conversion rate of SO_2 molecules into particulate SO_4^{2-} . It was found that the relative amount of carbon black to total carbon increased with increasing engine thrust while mass emission of particulate sulfate remained almost constant.

The study presented by Rai et. al. [26] compares LIBS to atomic emission spectroscopy (AES) for detection of metal-seeded aerosols in hydrocarbon flame and rocket engine simulator plume. Their goal included developing a system to act as a health monitor for the engine allowing engine shut down prior to catastrophic failure. Past catastrophic engine failures record intense optical emission preceding the event. The benefits of LIBS for this application include real-time analysis, small sample requirement with no sample preparation, operation in harsh environments, and proven elemental sensitivity, shown in previous references. In this reference it was shown that LIBS signal for metal-seeded plumes decreases in the luminous flame region, possibly due to higher background emission from the flame. The same result occurred in testing of the rocket

engine simulator plume of decreased signal in the luminous zone near the nozzle exit. The conclusion of this study suggested that LIBS might be capable of detecting trace metals from engine wear, thus to act as an engine health monitor, demonstrating the ability to sample directly in extreme temperatures of ~2000K.

CHAPTER 3 Apparatus and Procedure

The LIBS configuration described in the following section was used in the experimental collection of data at the University of Maryland campus laboratory. A second setup not described in this report was constructed for field testing at Arnold Air Force base in Tennessee. The field system closely resembled the university system in order to maintain similar characteristics.

3.1 LIBS Apparatus

A schematic for the general LIBS experimental setup used during these experiments is shown in Figure 3.1.1. Letters in parentheses in the text to follow refer to items in the Figure. A Quantel Brilliant Q-switched Nd:YAG laser (A) operating at

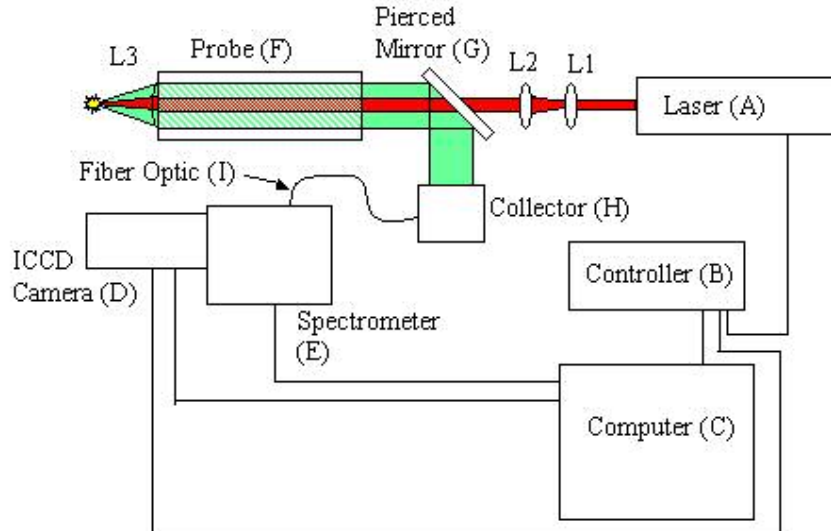


Figure 3.1.1 - Generic LIBS experimental apparatus.

1064 nm wavelength and delivering energy up to 360 mJ per pulse, with a repetition rate of 10 Hz and pulse width of ~5 ns, was used to generate the plasma spark. The laser

beam leaves the optical laser head with diameter ~3-4 mm and passes through two lenses (L1, a 1" diameter concave lens with focal length -29.1 mm and L2, a 1" diameter convex lens with focal length 143.2 mm) acting as a Galilean expansion telescope producing a beam diameter of ~12-14 mm. All of the lenses used in the setup are UV grade fused silica. The infrared beam (shaded darker in Figure 3.1.1) then passes through a 0.5" hole drilled at a 30° angle in a 4" diameter mirror, hereafter referred to as the pierced mirror (G). The beam is focused in the exhaust plume at the end of the sampling probe by a 2" diameter, 75 mm focal length lens (L3). The breakdown spark emission is collected and collimated by the same focusing lens, L3, and returned through the sampling probe to the pierced mirror. The pierced mirror reflects the signal, minus that lost through the hole in the mirror, to an achromatic collector/collimator, CC52, from Multichannel Instruments (H). The collector focuses the signal light onto the circular end of the fiber optic bundle (I), which threads into a cylindrical sleeve on the collector. The fiber bundle is composed of 19 single fibers of core diameter 0.2 mm. The fiber is 3 m long and can transmit light from 190-1100 nm wavelength. One end of the fiber is configured with a circular SMA905 connector to thread onto the collector and accept the LIBS signal. The opposite end is composed of a 10 mm diameter ferrule housing the individual fibers arranged in a single row to couple the signal to the imaging spectrometer.

The spectrometer is a SpectraPro-300i (E) from Acton Research Corporation with a 0.3 m Czerny-Turner design and a triple grating turret which accepts up to 3 gratings, selectable by computer software. While three gratings were present in the spectrometer, the experiments were performed with grating containing 1200 grooves/mm, corresponding to 26 μm/pixel. A 1024x256 element intensified charge-coupled device

(ICCD) Princeton Instruments, PI-MAX Camera (D) was the detector mounted at the exit of the spectrometer to record the spectrum. The spectral region visible to the detector was ~ 40 nm when using the 1200 g/mm grating. The ICCD detector operated in gated mode and was synchronized to the laser Q-switch through the Princeton Instruments Controller, ST-133 (B), which housed a plug-in programmable timing generator (PTG) by Princeton Instruments designed to operate specifically with the ST-133 Controller. The Q-switch allows lasing to begin and acts as an external trigger for the PTG, which controls the gate pulse of the ICCD detector. The gate delay controls how much time elapses between the Q-switch trigger and the opening of the detector shutter, and gate width is the duration that the shutter remains open. The gate delay and width are computer controlled and are unique to each element sampled due to emission physics described in Section 2.1; these were optimized experimentally for each element to maximize the P/B ratio. Data acquisition and analysis were performed using a personal computer (C) with Princeton Instruments WinSpec spectroscopic software. The software can control the spectrometer turret and detector gate width and delay settings described previously. WinSpec can also define a predetermined number of single shot spectra to be accumulated into one spectral file. An accumulation of n spectra represents a sum of the spectral intensities from n signals into one spectral image. Large sets of single shots can also be stored individually in WinSpec.

3.2 Sampling Probe

Due to the forthcoming application in the harsh environment created by the high temperature turbine exhaust plume, a sampling probe (F) was designed to extend the measurement volume into the exhaust plume, while allowing distance between the exhaust plume and the sensitive LIBS equipment. The probe was designed and built in-house and is comprised of two concentric stainless steel pipes that are 3' long with 2" and 3" diameters. The 2" diameter pipe is placed inside the 3" diameter pipe and annular plates welded to the ends of both pipes connect them together. A 1/2" annular region is sealed between the concentric pipes and annular end caps leaving the 2" diameter pipe open at both ends.

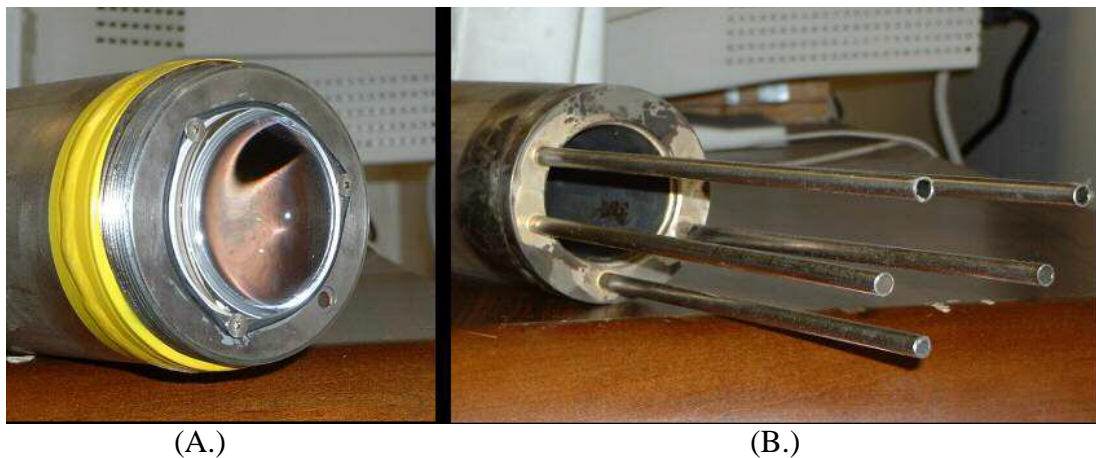


Figure 3.2.1 - (A.) shows probe end containing laser focusing/emission collection lens. (B.) shows opposite probe end with five tubes for inlet and outlet cooling water, and one for nitrogen lens purge. End cap that protects lens in exhaust plume is not pictured.

At the end of the probe closest to the laser, five 1/4" diameter stainless steel pipes enter into the annular endplate. Two of these pipes extend almost the length of the probe to the annular plate at the sampling end. These two pipes channel the flow of cooling water to the lens region, supplying the water to the annular cavity near the lens. The

water then flows back to the end where two of the five 1/4" pipes serve as an outlet for the cooling water. The fifth 1/4" diameter pipe extends to the far annular endplate and opens directly adjacent to the focusing lens. This pipe carries dry air that exits next to the focusing lens and purges the end cap, minimizing exposure of the lens to high temperatures and combustion products.

At the sampling end of the probe, the 2" diameter opening is used to house a fused silica lens, which has a 2" diameter and focal length of 7.5 cm. The lens is secured in the opening with a retaining bracket that is screwed onto the annular plate. The outer pipe is threaded at the sampling end in order to accommodate an end cap that acts to protect the focusing lens. The end cap threads onto the outer pipe and the air from the fifth 1/4" pipe blows into the end cap, acting as a clean air purge. The air exits the end cap through a 1/2" hole centered directly in front of the lens. The end cap hole size is large enough to allow all light from the plasma spark to be collected by the lens and returned to the collection optics, but small enough that the dry air flow rate is enough to keep a higher pressure in the end cap than outside the end cap. This ensures that unfiltered air from the sampling environment cannot enter the end cap and possibly deposit particles on the lens or damage the optics.

3.3 Aerosol Generation

The calibration of the LIBS system required aerosol generation to simulate the particulate to be detected in the gas turbine exhaust. The aerosol was generated using a setup that incorporated a modified commercially available atomizer (TSI Constant Output Atomizer Model 3076) coupled with a Razel Model A-99 Syringe Pump. Figure 3.3.1

shows the atomizer with the associated syringe pump and compressed air supply line. The atomizer consists of an atomizer assembly and reservoir, and can operate in both recirculating and non-recirculating modes. The non-recirculating mode was used for this experiment, requiring a syringe pump to supply fresh solution to the atomizer. In the recirculating mode, solution for atomization is supplied from the excess drain off container. The recirculating configuration was not used in these experiments due to the possibility of increasing elemental concentration in the solution with time, as the solvent could evaporate and exit the container through the pressure relief valve, resulting in decreasing solvent volume and thus increasing concentrations of solute. A diagram of the atomizer assembly is shown in Figure 3.3.2.

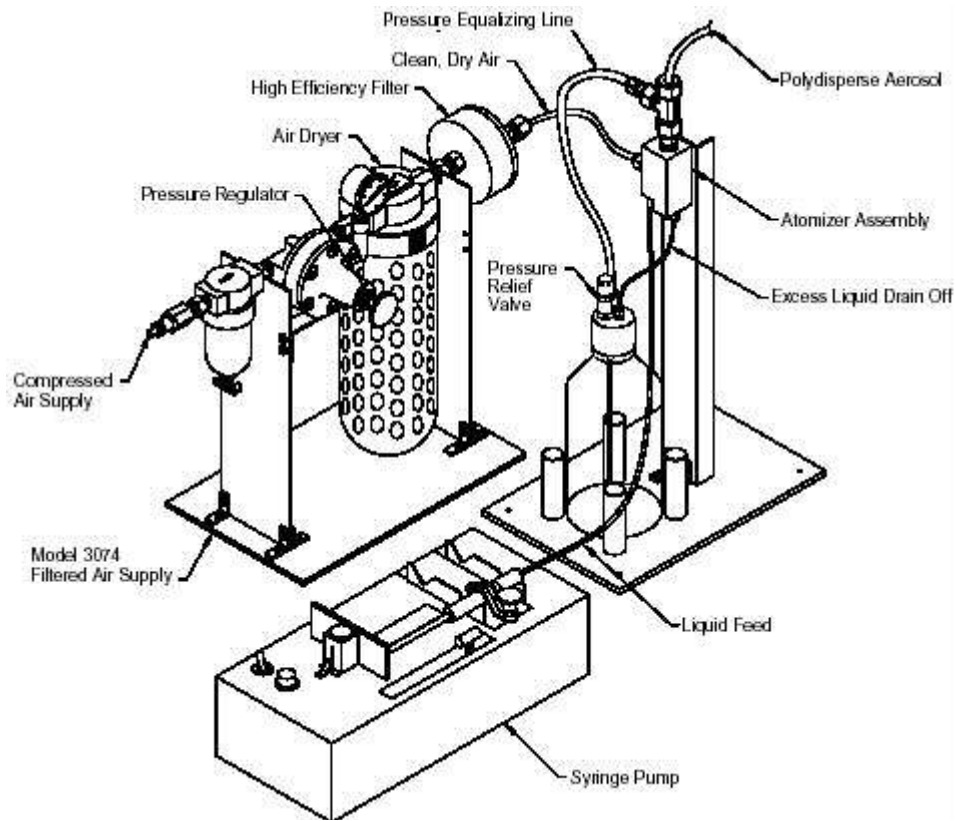


Figure 3.3.1 - TSI 3076 atomizer with syringe pump[32].

Referring to Figure 3.3.2, the aerosol is formed by injecting a stream of clean, dry, compressed air through an orifice at approximately 1 L/min perpendicular to the inlet of the aqueous metal solution. This high velocity jet blows over the opening of the vertical channel supplying solution, creating a spray of droplets. Large droplets have a high Stokes number and are not able to follow the air jet in a 90° turn upwards, and thus they are filtered out by impaction against the wall opposite the jet. Smaller droplets have small Stokes numbers and are able to follow the air jet to the aerosol outlet. The excess liquid from the impacted droplets is then collected in the closed reservoir below the

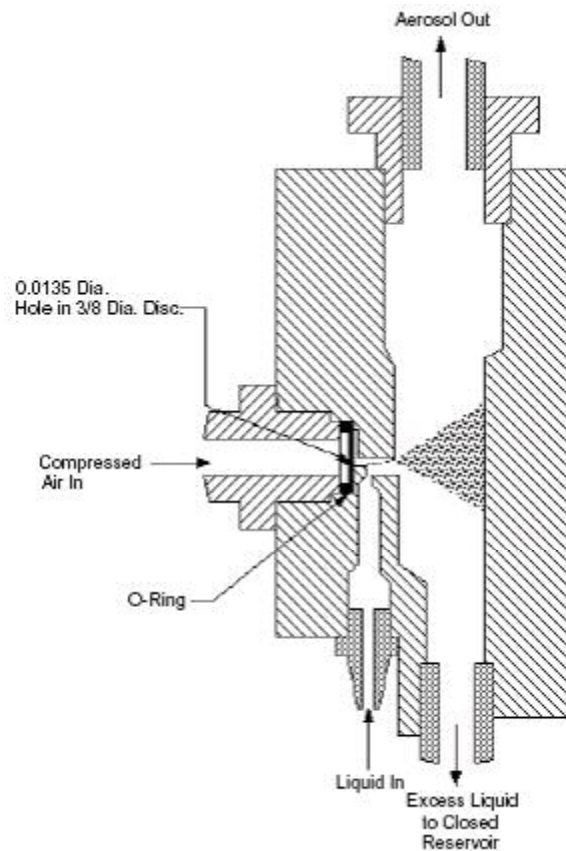


Figure 3.3.2 - TSI 3075/3076 atomizer assembly [32].

assembly. Collection and measurement of the excess liquid from the reservoir revealed that approximately 10% of the injected aqueous solution entered the diffusion dryer. A

second compressed air inlet for dilution air is introduced following the atomizer using a T-junction fitting. This dilution stream allows the concentration of the aerosol to be increased or decreased by changing the dilution air flow rate. The atomizing air stream flow rate was controlled with a rotameter (N044-40) with a steel float and the dilution air stream flow rate with a rotameter (N102-05) with a steel float, both from Cole-Parmer Instrument Co.

The generated aerosol particles carry electrostatic charge. A special conductive silicone tubing was used to transport the aerosol to the sampling region. The conductive silicone reduces the buildup of static charge, minimizing the particle losses to the tube wall. The entire assembly generates sub-micron sized aerosols with a number median diameter liquid droplets from the atomizer of approximately $0.3 \mu\text{m}$ and a geometric standard deviation less than $1.9 \mu\text{m}$. The aerosol is dried in a custom diffusion dryer. The mean particle size of the final aerosol varies between 0.02 and $0.3 \mu\text{m}$, depending on solution composition [32].

Characterizing the exact aerosol number size distribution of the atomizer required the use of a TSI Model 3081 long tube Differential Mobility Analyzer (DMA) coupled with a TSI Ultrafine Condensation Particle Counter (CPC) Model 3025A. The DMA, discussed in depth by Knutson and Whitby [33], is an electrostatic classifier that selects particles based on electrical mobility by balancing the electrodynamic and aerodynamic forces on particles that enter. The instrument consists of a center rod that carries a high voltage and a larger diameter housing cylinder that contains the center rod. Clean, dry air, referred to as sheath flow, flows through the housing cylinder, and charged polydisperse aerosol is introduced at the outer wall of the housing column. It is crucial

that the sheath flow and polydisperse flow have equal velocity to minimize shear induced vorticity and mixing during the merge. The axial sheath flow carries the polydisperse particles toward the bottom exit of the DMA while the electric field generated by the high voltage center rod attracts the charged particles toward the center from the aerosol layer at the outer wall. Particles with high electric mobility impact the center rod upstream of the sampling slit and those with low mobility are carried out the main exit with the sheath flow. Depending on the DMA voltage, a narrow range of particles possess the mobility to be carried into the sampling slit located on the center rod.

Knutson and Whitby discuss the development of a transfer function, Ω , for the electrostatic classifier, which is the probability that a particle with mobility Z_p that enters the DMA will exit via the sampling slit. A band of particle sizes will enter the sampling slit for given values of applied voltage on the center rod and flow rates through the classifier. The centroid of the mobility band, Z_p^* , can be calculated by Equation 3.1 was used in an Excel database with a range of particle diameters as input. Two equations for Z_p^* allow for the calculation of the mobility band centroid based on either voltage, V , or

$$Z_p^* = \frac{(q_c + q_m)}{4\pi\Lambda V} \quad (3.1)$$

$$Z_p^* = \frac{qC_c}{3\pi\mu d_p} \quad (3.2)$$

where

$$C_c = 1 + K_n \left[A + B \exp\left(\frac{-C}{K_n}\right) \right], \text{ Cunningham slip correction factor,}$$

$$K_n = 2\lambda/d_p,$$

$$\Lambda = \frac{L}{\ln(r_2/r_1)},$$

$$q = ne,$$

$e = 1.6 \times 10^{-19}$ Coulombs, a single unit of electrostatic charge,
 $n = 1$, number of charges on particle,
 $\eta = 1.807 \times 10^{-5} Pa \cdot s$, viscosity,
 d_p = particle diameter, and
 $\lambda = 0.0665 \mu m$, mean free path at STP.

particle diameter, d_p . For each particle diameter, the Cunningham slip correction factor is calculated. The slip correction factor and particle diameter are substituted into Eq. 3.2 and the centroid of the mobility band is determined. The centroid is substituted into Equation 3.1 to solve for voltage, V , obtaining the DMA voltage setting corresponding to specific particle diameters. From this analysis, the minimum and maximum particle sizes that pass into the sampling slit are given by

$$Z_{\min} = \frac{(q_c - q_s)}{2\pi\Lambda V} \quad (3.3)$$

$$Z_{\max} = \frac{(q_a + q_c)}{2\pi\Lambda V} \quad (3.4)$$

where q_a = aerosol flow rate,
 q_c = clean air flow rate (sheath flow),
 q_m = main outlet flow rate, and
 q_s = sampling flow rate.

The dried particles from the DMA enter the CPC and pass through a capillary tube and into a saturator region. Vapor diffuses to the dry flow from a saturated sheath flow of air. Vapor condenses rapidly on the aerosol particles as the saturated flow passes through a cooled condenser, forming droplets around the particles. The droplets are then counted individually by scattered laser diode light collected by a photodetector. Figure 3.3.3 shows that CPC detection efficiency approaches 100% for particle diameters greater than 5 nm, which includes all particles of interest in this study.

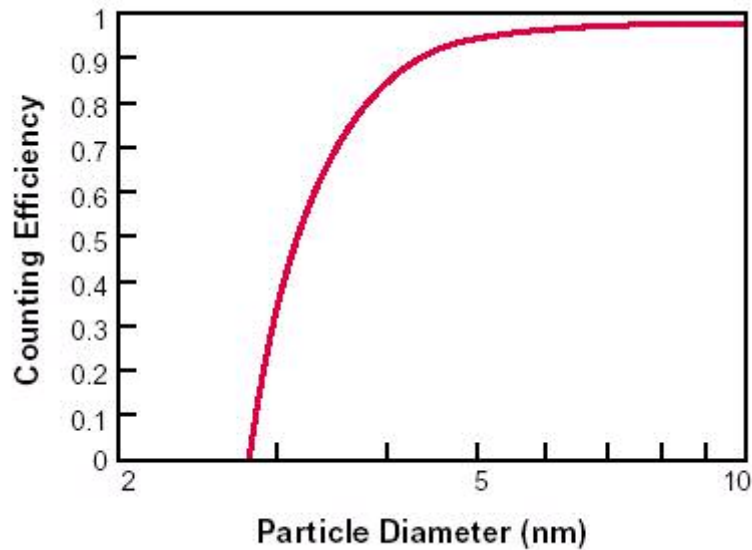


Figure 3.3.3 - Particle detection efficiency, NaCl particles in nitrogen at 1500 cm³/min inlet flow.

3.4 Flow Reactor

The flow reactor, Figure 3.4.1, is a combustion flow apparatus that provides combustion products for performing calibration testing in the University of Maryland laboratory. It is a tubular reactor with a sampling region and a moveable, removable injector that holds a flame. The reactor is an L-shaped stainless steel tube with a 30" horizontal run, followed by a 90° elbow forming a bend and a 16" vertical run. The horizontal length holds the flame injector, therefore only exhaust is traveling through the vertical section. The vertical section incorporates a cross-shaped test section with clear windows on three of the four cross-pipe ends. The fourth end acts as a beam dump after the sampling region. Air lines are connected to the cross-pipes next to the windows to purge them of particulate and prevent condensation from forming due to the temperature difference between the exhaust flow and the ambient lab temperature. The vertical pipe ends 10" above the cross test section and the exhaust flows into a vacuum hood to be

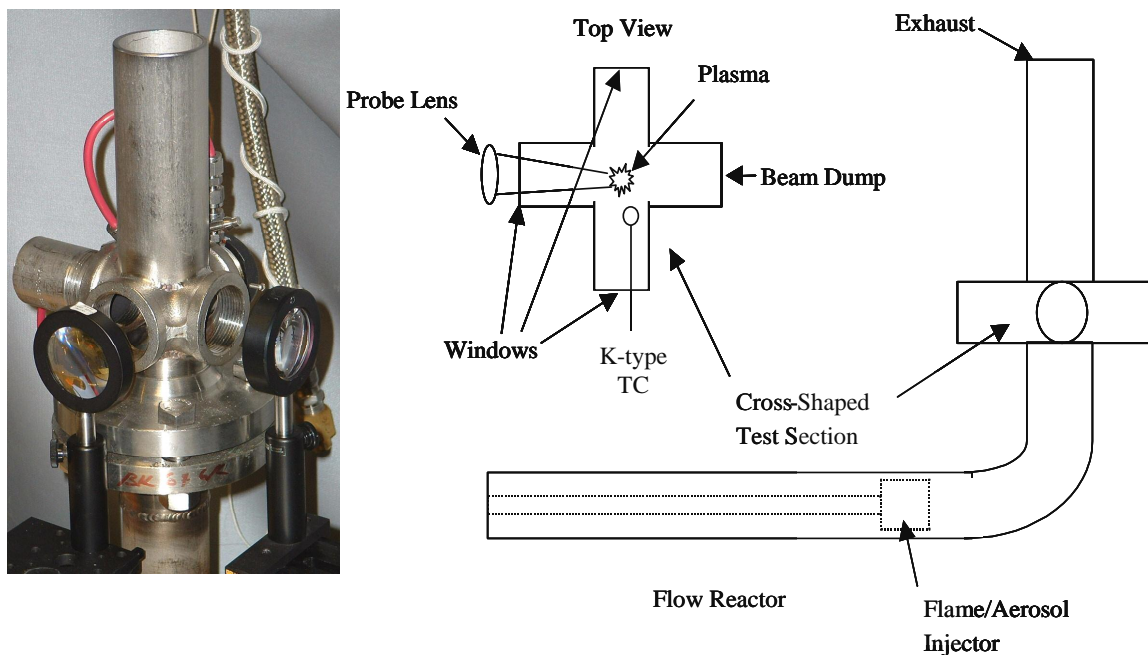


Figure 3.4.1 - Flow Reactor with detailed view of cross-shaped test section.

removed from the lab. The test section allows sampling without entrainment of ambient air. The flame injector is a cylinder that fits tightly in the horizontal section of the flow reactor chassis. The cylinder is about 2" in diameter and 2" long and composed of steel. The center is packed with glass beads and held in place with a mesh screen. The beads act to diffuse the air/fuel premix that enters the cylinder at two locations on the same face. Between the two entrances for the premix is a third passage through the entire cylindrical injector head. This passage accepts the tube that carries the aerosol into the flame. The opposite face of the cylindrical injector has a pattern of holes to allow the premix to exit into the flame region. The flame holder (injector) is ignited with a lighter outside of the flow reactor and then inserted in the horizontal section. The injector head is pushed until it reaches the elbow in the chassis. The fuel used in the flow reactor is typically propane.

3.5. Experimental Procedure

Experimental set up included an extended stage of optical alignment of the pierced mirror and the sampling probe. Optimal alignment was achieved by monitoring the intensity of the carbon emission peak at 247 nm during adjustment of the optics. Carbon occurs naturally in the air, principally as CO₂, eliminating the need to seed the flow during the optical alignment process.

Determining the optimal detector gate width and delay to maximize the P/B ratio for each element was the next step in calibration of the system. Preliminary test runs involved broad time sweeps in an effort to determine timing ranges for each element. Each of the four elements, Cr, Mg, Mn, and Ti, were atomized and injected into the plasma sample volume directly from the TSI atomizer. Data collection took place at delay and width times suitable for locating the optimum P/B ratios for each element. Fifty single-shot spectra were obtained and averaged in Matlab to determine the combination of gate width and delay that produced maximum P/B ratios. Preliminary results showed that, in general, longer gate width intervals improved P/B ratio. Further tests, including 100 single-shot spectra per run at two laser energies of 30 mJ and 60 mJ per pulse determined the optimal delay times for each element. For all elements, the atomizing air flow was controlled by a rotameter at approximately 1.2 L/min, and the ICCD detector gain was set to 128 for Mg, and at 255 for other three elements. Table 3.5.1 provides the gate width and delay timing tested for each element to maximize P/B ratio.

It is desirable to optimize the P/B ratio for each element to obtain the best limit of detection. Determination of the LOD was accomplished with both polydisperse and

monodisperse aerosols, sampling from both at room temperature and 420°C. Therefore, a matrix of four test samples was collected and studied to compare the effects of aerosol character, aerosol concentration, and ambient temperature on the elemental LOD's for the LIBS apparatus.

	Laser Power (mJ)	Width (µsec)	Delay (µsec)
Cr	30	5, 10, 15, 20	4, 8, 12, 16, 20, 24
	60	15, 20, 25, 30	12, 18, 24, 30, 36, 42
Mg	30	10, 15, 20, 25	0.25, 0.5, 0.75, 1, 2, 3, 4, 6
	60	10, 15, 20, 25	0.5, 1, 2, 4, 8, 12, 16
Mn	30	10, 20, 30, 40	5, 10, 15, 20, 25, 30
	60	10, 15, 20, 25	5, 10, 15, 20, 25, 30
Ti	30	5, 10, 15, 20	0.5, 0.75, 1, 2, 4, 6, 10
	60	5, 10, 15, 20	0.5, 1, 5, 10, 15, 20

Table 3.5.1 - Detector gate width and delay ranges tested for each element.

Polydisperse LOD data collection involved seven test runs for each element, accumulating 500 single shot spectra, with aerosol concentration decreasing on each successive run. The polydisperse aerosol exited the diffusion dryer and clean, dry dilution flow was introduced to the stream to adjust the aerosol concentration before entering the sampling region. Room temperature LIBS sampling occurred directly from the exit of a carrier tube apparatus that injected the aerosol flow through a 3 mm diameter tube into the plasma spark at a flow rate that varied with the level of dilution flow. The process was repeated with seven runs for each element at an elevated gas temperature of 420°C. In both room temperature and heated test runs, Mg was diluted with a higher flow rate than the other three elements, resulting in lower Mg aerosol concentrations at the sampling points due to the higher Mg signal strength. The apparatus in the heated test run involved adding a high flow rate Bunsen burner under the aerosol injection tube. The luminous region of the propane-air premixed flame from the burner was just below the

aerosol carrier tube, allowing the aerosol to be heated by the high temperature exhaust plume without turbulent mixing which could decrease metal concentration. A K-type thermocouple was positioned approximately 1 cm from the plasma spark to obtain aerosol stream temperature at the sampling height above the burner.

Monodisperse aerosol sampling was similar in procedure to the polydisperse testing previously described. The apparatus differed in that the polydisperse aerosol flow was carried from the diffusion dryer to the DMA where a voltage was set to select a certain range of particle sizes from the polydisperse flow. The monodisperse aerosol that left the DMA was carried directly to the injection tube described previously. Measurements at room temperature, 21°C, involved making 4 test runs for each element. For each monodisperse aerosol concentration, 1000 single shot spectra were taken. The concentration was decreased in each successive test run by increasing dilution flow rate. The sampling in the exhaust at 420°C occurred in the same way, except the monodisperse aerosol injected into the exhaust stream of the Bunsen burner as described above. The operation of the DMA to generate monodisperse aerosol required slight differences between the elements due to the fact that the particle size distribution for each element was slightly different. The applied voltage on the center rod of the classifier was chosen based on acquiring the mobility band that contained the largest mass concentration of the elements. Furthermore, the ratio of sheath flow to polydisperse flow was changed for Mn, Cr, and Ti. The ratio of sheath-to-polydisperse aerosol flow determines the half-width of the mobility band. A narrow band width generated by a sheath-to-polydisperse ratio of 10:1 worked for Mg since it has the strongest emission signal of the four studied elements. But for Cr, Mn, and Ti the sheath-to-polydisperse ratio was changed to 5:1 to

allow a wider range of particle sizes to enter the sampling slit of the center rod in the DMA to increase the concentration and hence the LIBS signal. The operating settings for the electrostatic classifier are given below in Table 3.4.2 based on element to be sampled.

Element	Sheath Flow Rate (L/min)	Voltage (V)	Particle Diameter Centroid, dp (nm)	Monodisperse Concentration Undiluted (fg/cc)
Cr	5	1.982	170	17988
Mg	10	3.244	150	2671
Mn	5	1.8	165	19039
Ti	5	1.982	170	117808

Table 3.5.2 - Classifier settings and resulting monodisperse concentrations.

CHAPTER 4 Experimental Results

The following sections detail experimental results used to compare calibration curves and limits of detection for the LIBS system. The effects of variations in both ambient sampling temperature and aerosol dispersity are presented.

4.1 Calibration

Calibration of the system first requires precise alignment of the optical configuration to ensure maximum collection of light from the plasma. This is accomplished experimentally by collecting spectra while modifying the optics and comparing elemental peak intensity, typically using the 247 nm C line from naturally-occurring CO₂ in the air, as discussed in Chapter 3. The highest achievable optical signal (i.e. strongest spectra possible) is desired from the optical setup before beginning the calibration process.

After the optical alignment, the optimal detector gate width and delay is determined for each element. Figure 4.1.1 below shows a scan over a range of different gate delays, with each curve representing constant gate width, both values in μsec . The plot shows P/B ratios for polydisperse Cr aerosol that was generated by using the TSI atomizer described in the Section 3.3. The aqueous Cr solution was injected at a flow rate of 33.3 cc/hr and the impinging air jet had a volumetric flow rate of approximately 1 L/min. The droplets were passed through the diffusion dryer to evaporate the solvent, leaving Cr particulate to be carried in the air stream to the sample volume. Each data point represents an average of 100 single-shot spectra taken at the prescribed gate width and delay. The P/B ratios in this plot are higher than P/B ratios calculated in later

experiments during calibration due to the use of a much higher analyte concentration. This flow was heavily seeded with polydisperse aerosol, ensuring consistent elemental presence in the sample plasma volume. The profiles shown in Figure 4.1.1 provide insight into the effects of varying gate width, delay and laser power on P/B ratio. Lines in the figure serve only to connect the points that represent the data. Values of gate width (μs) and laser power (mJ) are provided in the legend.

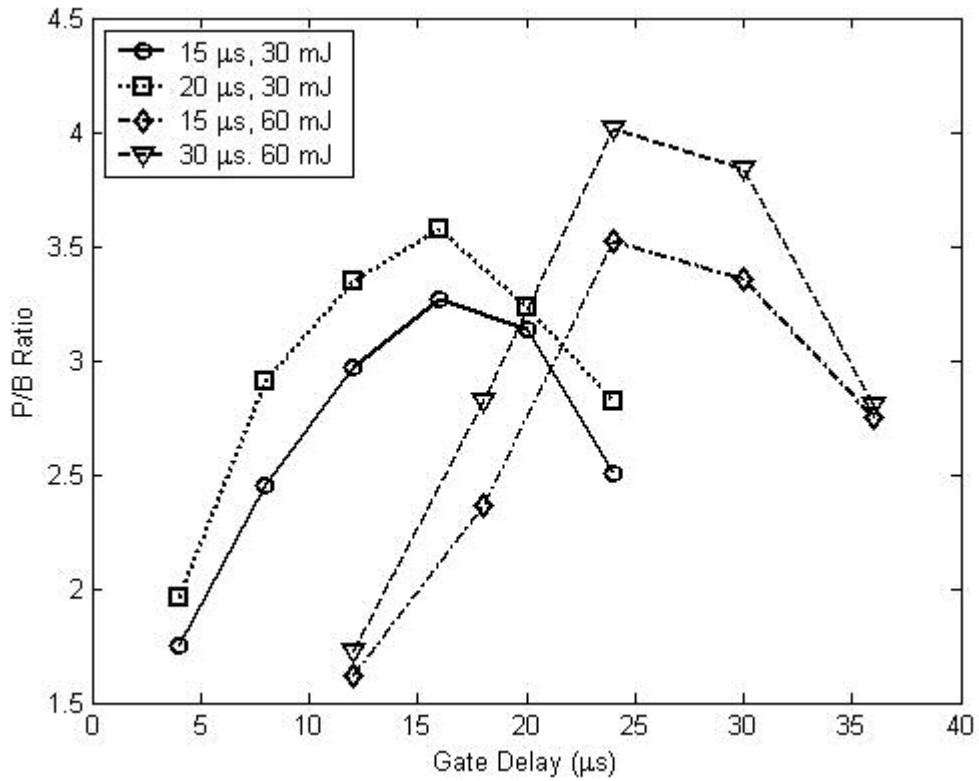


Figure 4.1.1 - Chromium aerosol particles, gate width and laser power indicated in legend.

Analyzing Figure 4.1.1, the maximum P/B ratios occur at delays of 16 μs with a laser power of 30 mJ and around 24 μsec with a laser power of 60 mJ for both gate widths shown in the figure. The optimal delay is longer when the laser pulse energy is higher due to a higher plasma temperature. As discussed elsewhere (Fisher et. al. [15])

the optimal delay is a function of energy of the transition and the temperature of the plasma. The energy of the laser pulse primarily affects the size of the plasma, which in turn affects the plasma cooling rate, through surface-to-volume considerations. The gate width had a noticeable effect on the measured P/B ratio as a longer gate width exposes the detector to the analyte emission for more time. At both laser powers, the longer gate width increased the average P/B ratios at each gate delay setting. The standard deviation calculated from the 100 single shot spectra corresponding to each experimental condition of Figure 4.1.1 is shown in Fig. 4.1.2. The standard deviation remains relatively uniform and relatively large across the four curves, due to significant fluctuation in the shot-to-shot P/B ratios.

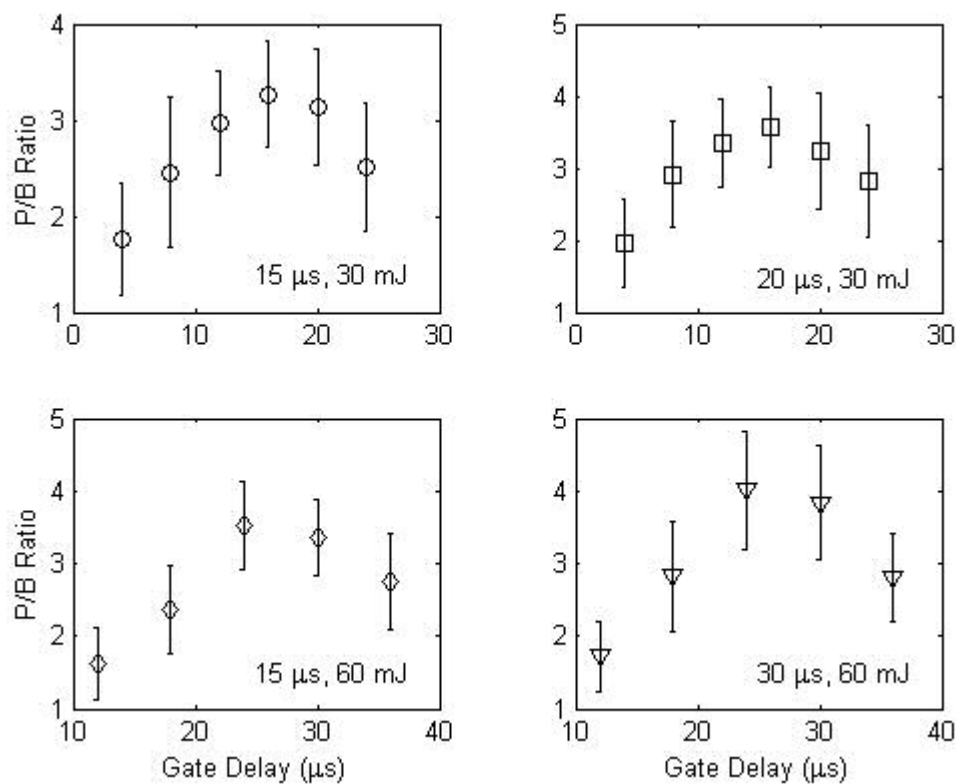


Figure 4.1.2 - P/B ratio curves from Fig. 4.1.2 with error bars representing +/- 1 standard deviation.

Detector gate width and delay adjustment offers a powerful tool for maximizing P/B ratio in varying sampling environments. The timing measurements shown above are from spectra taken with clean, compressed air as the aerosol carrier stream. At longer times, spectra taken in engine exhaust carrying particulate will include strong molecular bands resulting from recombination of elements present in the combustion products. Rai [26] et. al. show two spectra, one taken in air and the other in a hydrocarbon flame, both seeded with aerosol mixtures of iron, chromium, and nickel. Strong elemental peaks were clear for all three elements in the spectra taken in air. However, only iron peaks were visible in the hydrocarbon flame spectra. This is either due to depletion of elemental concentration from thermal and chemical effects or relatively stronger peaks that conceal the elemental peaks. The latter case could possibly be corrected by determining the gate width and delay that maximize the elemental peaks and minimize the background peaks.

While data was taken at both 30 mJ and 60 mJ pulse energies to study the effect on the P/B ratio, further testing was conducted using only a laser pulse energy of 60 mJ so that a higher temperature plasma spark was created, thus increasing the magnitude of the average P/B ratios. Data such as that in Figure 4.1.1 allows determination of optimal

Element	Gate Width (μsec)	Gate Delay (μsec)
Cr	30	24
Mg	25	1
Mn	30	20
Ti	20	10

Table 4.1.1 - The optimum detector gate width and delay times.

gate width and delay for obtaining maximum P/B ratios; and was collected for the four elements of interest. Table 4.1.1 provides the width and delay used in subsequent experiments (unless otherwise stated).

4.2 Aerosol Dispersity

The aerosol generation system is described in detail in Section 3.3, above. Accurate assessment of the mass concentration of analyte in the carrier stream requires knowledge of the aerosol particle size distribution in the experiment. Aerosol is produced by the nebulizer using standard ICP solutions, and is subsequently dried in the diffusion dryer. The aerosol exiting the diffusion dryer enters the DMA, which outputs a monodisperse aerosol of known diameter. The concentration of particles per cubic centimeter is quantified by the CPC. Three particle concentration measurements from the CPC are recorded for each size (voltage setting on the DMA) and these are averaged to determine the particle concentration at a specific diameter. The number concentrations were corrected by first doubling the values measured by the CPC. The DMA charges the polydisperse aerosol equally with positive and negative charges, but only attracts and collects negatively charged particles due to the positive charge on the inner rod. Therefore roughly half of the particles in each size category are lost to the DMA waste exit stream.

The next step in accounting for the concentration losses due to the DMA is a Boltzmann charging correction calculated for each particle diameter [34]:

$$f(n) = \sqrt{\frac{e^2}{dkT\pi}} \exp\left(\frac{-n^2 e^2}{dkT}\right) \quad (4.1)$$

where $e = 1.6 \times 10^{-19}$ Coulombs, a single unit of charge,
 $n = 1$, number of charges on particle,
 $k = 1.381 \times 10^{-16}$ erg / K , Boltzmann's constant,
 d = particle diameter, and
 T = temperature.

The doubled number concentrations are divided by the Boltzmann charging coefficients. This correction is only valid for particles with diameter 50 nm and larger, which includes all of the sizes of interest in this study; the correction is significant for large particles. Figure 4.2.1 shows the measured particle size distributions for the four elements of interest on a logarithmic x-scale. This figure illustrates the expected roughly log-normal distribution of aerosol from the nebulizer, with little variation in mean size for aerosols of various metals; the mean particle diameter, D_p , was approximately 40 nm for the four elements. Due to the size limitation of the charge correction, the data shown in Figure 4.2.1 is the number concentration doubled, but not corrected with the Boltzmann charge coefficient. With or without the correction the size distribution is roughly log-normal.

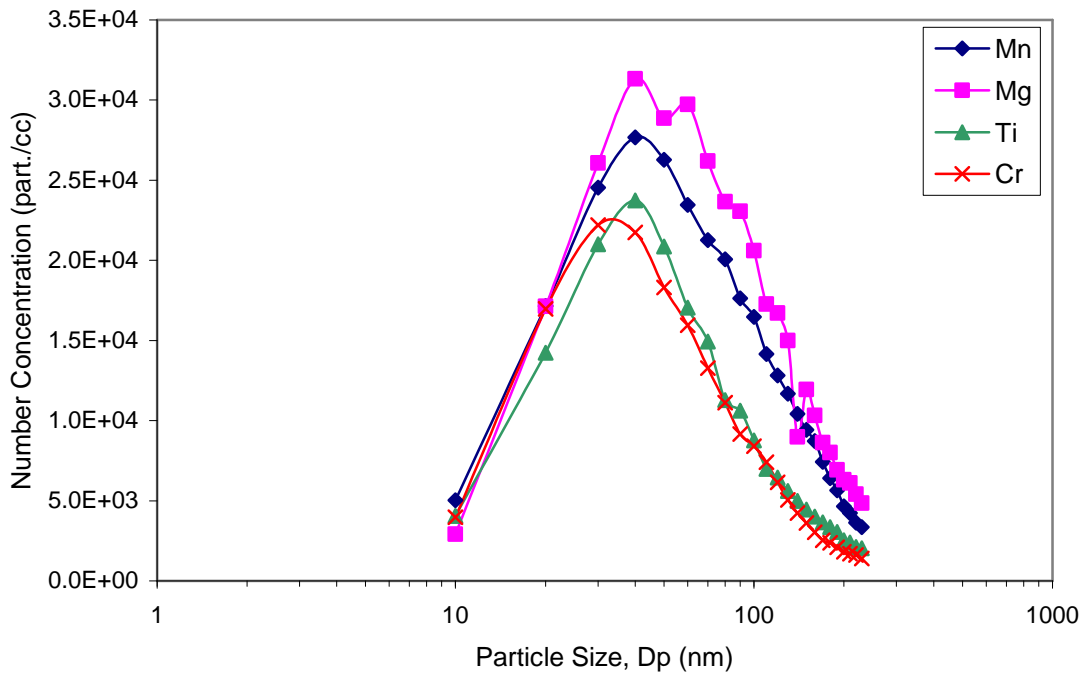


Figure 4.2.1 – Particle size distribution of Cr, Mg, Ti, Mn.

The mass distribution of the polydisperse aerosol is determined by multiplying the particle number size distribution by the mass of the element per particle. The four elements of interest are generated from aqueous solutions containing the following compounds: magnesium nitrate hexahydrate, manganese nitrate hexahydrate, titanium metal, and potassium dichromate. The solutions, obtained from Fisher Scientific, are mixed at 1% by weight of each compound. The titanium solution includes <5% hydrochloric acid suspended in water. The densities and molecular weights of the four compounds enabled calculation of the percent by mass, and ultimately the total mass concentration of Mg, Mn, Cr, and Ti given in Table 4.2.1.

Element	Total Elemental Mass Concentration (fg/cc)
Chromium	4.39E+05
Magnesium	1.96E+05
Manganese	3.85E+05
Titanium	2.67E+06

Table 4.2.1 – Elemental quantities aiding in calculation of total mass concentration in polydisperse aerosol stream.

The total elemental mass concentration is the concentration in fg/cc of metal mass in the aerosol stream exiting the diffusion dryer. This value determines the mass concentration injected into the plasma sample volume during calibration experiments, in which dilution flow is used to decrease the mass concentration. Calibration testing is performed with polydisperse and monodisperse aerosols; concentrations for the monodisperse aerosol are calculated with the same technique, but only a narrow particle size interval is considered.

4.3 Temperature Comparison

The limit of detection (LOD) varies between LIBS configurations due to many factors influencing the transmission and collection of the emission signal. Therefore, it is important to determine the detection limits with a particular LIBS configuration for the elements of interest before field testing begins. The primary aim of this work is to measure the effects of temperature and aerosol dispersity on the P/B ratio, and thus the elemental limits of detection. First, data was analyzed to decide what could be considered a particle hit. Matlab code was used to process sets of 500 single shot spectra taken in particle-free air. The measured P/B ratios at the location of each atomic line of interest were binned to determine the distribution of background P/B values due to noise. The process was performed for each elemental peak location; and on average it was found that 14.9% of blank single shot spectra had P/B ratio values in the range from 1.05-1.1, 3.04% of blank spectra produced P/B ratios in the range 1.1-1.5, and none were observed with P/B >1.5. Therefore, 100% of spectra with P/B ratios greater than 1.5 were classified as elemental hits, 97% with P/B ratios between 1.1 and 1.5 were hits, and approximately 85% were counted as hits if the P/B ratio was between 1.05-1.1. Spectra with P/B ratios below 1.05 were not considered as hits at all, because hits at this low threshold were well within the noise.

Figures 4.3.1 and 4.3.2 are histograms that illustrate the range of measured P/B ratios at room temperature and at high temperature. The binned P/B ratios in Figure 4.3.1 represent the aggregate of 500 single shot spectra of polydisperse Mn aerosol at room temperature. The P/B ratio is a monotonically increasing function of Mn concentration, and as a result, higher concentration flows have the measured distributions of P/B shifted

to the right. Figure 4.3.2 illustrates the aggregate of 500 single shot Mn spectra taken in the high temperature environment of the flow reactor apparatus discussed in Section 3.4. The P/B distribution measured for Mn at high temperature show a similar trend as that seen in Figure 4.3.1; the particle hit rates were lower. The bin numbers in Figures 4.3.1-4.3.3 correspond to P/B ratios as follows:

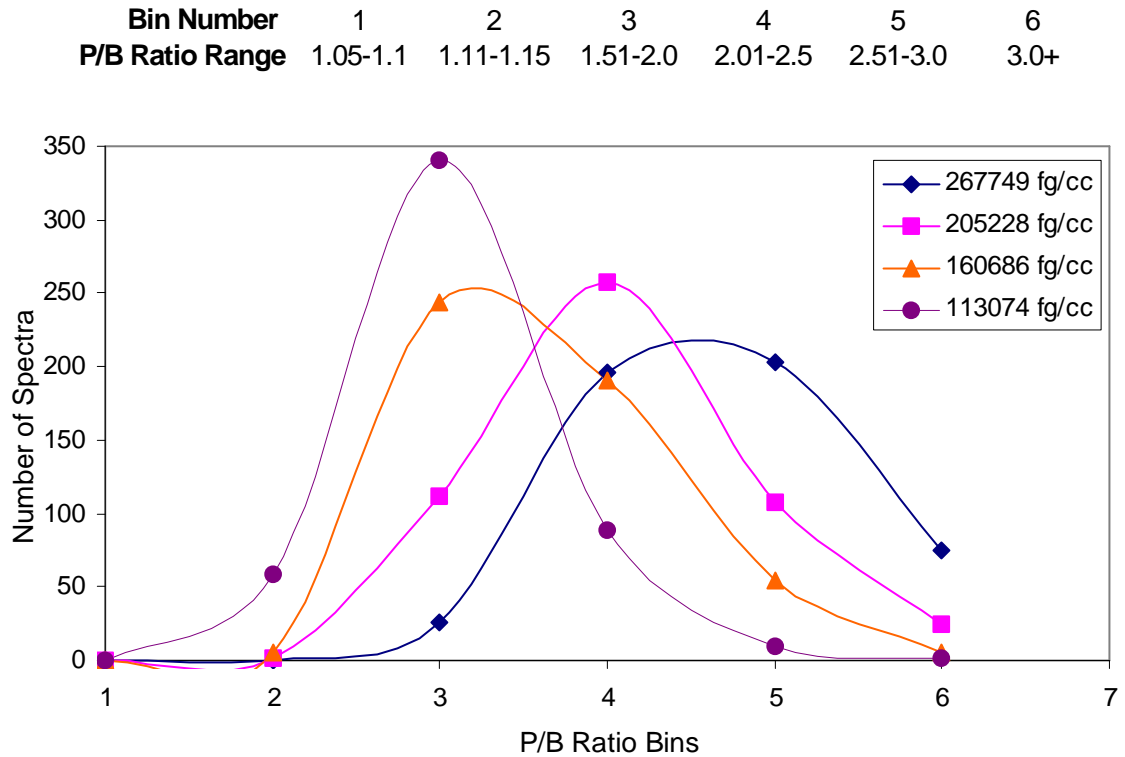


Figure 4.3.1 - Spectral hits binned by P/B ratio magnitude, polydisperse Mn at 21°C.

Figure 4.3.3 provides a direct comparison between high temperature measurements in the flow reactor (FR) and room temperature (RT) measurements, with an Mn concentration in the aerosol flow of approximately 110000 fg/cc. The lower sampling temperature data exhibits higher P/B ratios occurring more frequently. This could be an indication of thermal breakdown of metal particulate at combustion exhaust temperatures, resulting in size distributions where smaller particles dominate the

population. Other possible explanations for the lower P/B ratio observed in the combustion-driven flow reactor include the effects of changing gas mixture (chemical

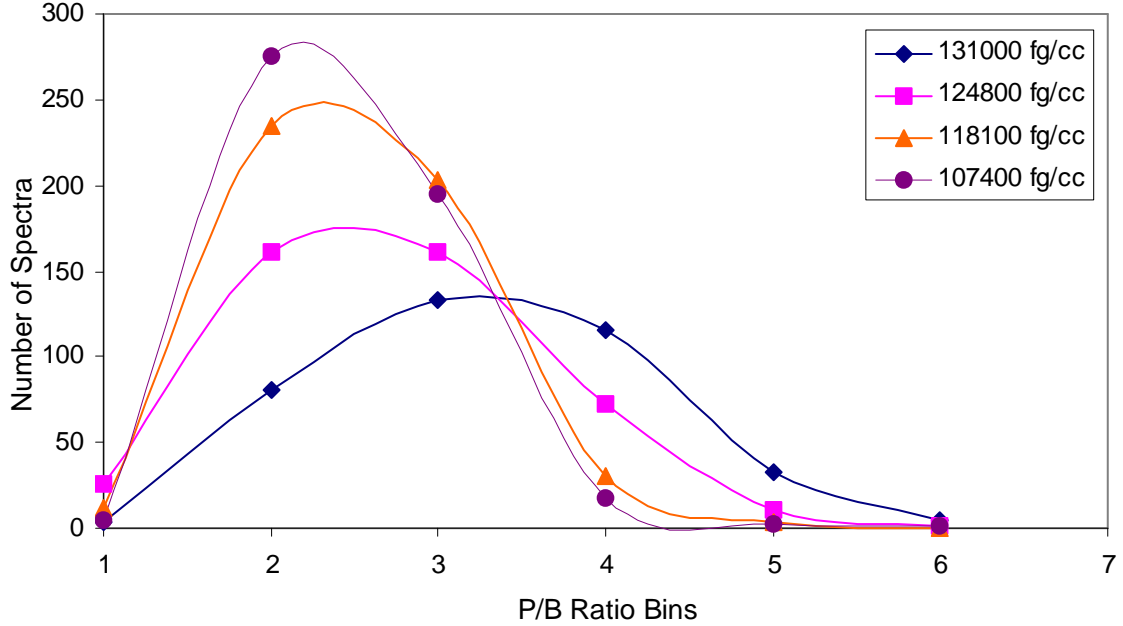


Figure 4.3.2 - Spectral hits binned by P/B ratio magnitude, polydisperse Mn at 420°C.

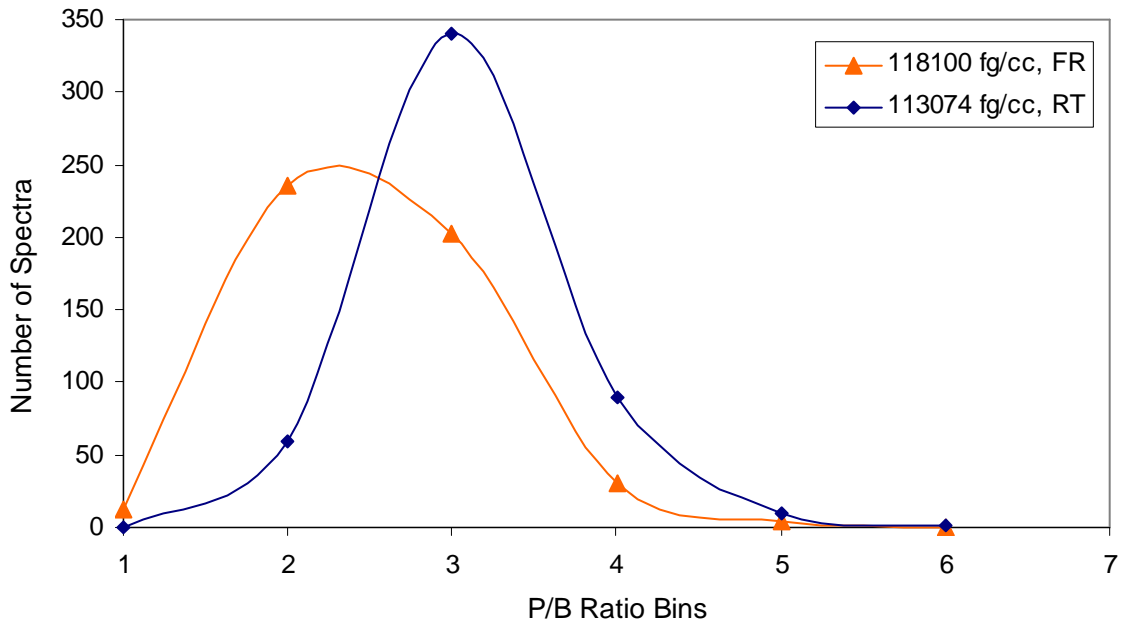


Figure 4.3.3 - Comparison of P/B ratio occurrences for polydisperse Mn.

quenching) or losses of particulate matter to the walls. In Figure 4.3.3, both the room temperature and high temperature data points were aggregates of 500 single shot spectra.

Figures 4.3.4-4.3.7 show the LIBS system calibration curves for each of the four elements of interest. Two sets of data are presented on the plots, one for room temperature data collection (circles) and one for sampling at elevated temperature in the flow reactor (squares). Each point represents the average P/B ratio taken from 500 single shot spectra as a function of aerosol concentration. The circles represent spectral data taken at room temperature and pressure. The temperature was maintained at approximately 420°C during the high temperature measurements to simulate the elevated temperatures of gas turbine exhaust in the sampling region of interest, reported by Arnold Air Force Base to be 382°-443°C. The error bars represent +/- 1 standard deviation from

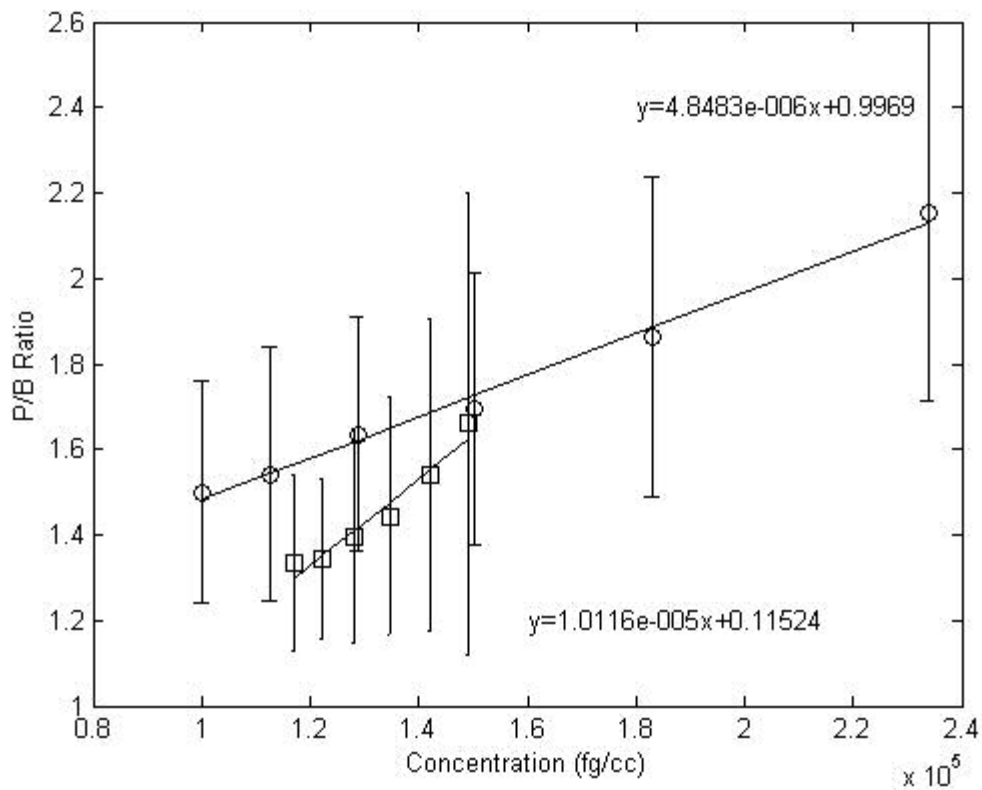


Figure 4.3.4 - P/B ratio as a function of Cr polydisperse aerosol concentration taken at room temperature (circles) and 420°C (squares).

the mean and are large due to the fact that the P/B averages were calculated based on all 500 single shot spectra, whether there was a hit or not. Additionally, the nature of polydisperse aerosol makes it highly probable that particles present in the plasma volume varied in size from shot-to-shot. The trend lines are linear regression fits to the data and are described by the two equations in the plots. The slope is necessary for calculation of the LODs.

Figure 4.3.4 shows that calibration curves for Cr are somewhat different with respect to temperature. The two P/B ratio magnitudes at a concentration of approximately 1.5×10^5 fg/cc are similar, while the high temperature data points decrease with concentration faster than the room temperature P/B ratios. For all measured Cr concentrations, the magnitudes of the high temperature P/B ratios were less than the P/B

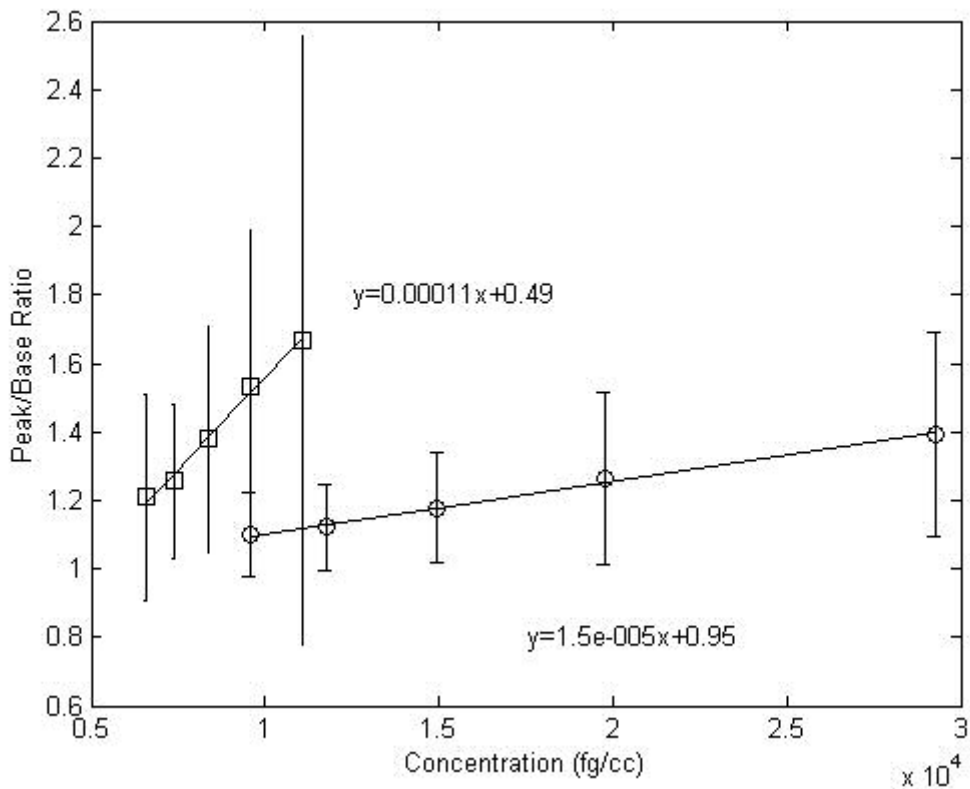


Figure 4.3.5 - P/B ratio as a function of Mg polydisperse aerosol concentration taken at room temperature (circles) and 420°C (squares).

ratios for the room temperature data. The error bars are consistent among the majority of points in both data sets. Figure 4.3.5 is unique among the plots comparing calibration curves, as Mg was the only element among the four tested (Cr, Mg, Mn, and Ti) that experienced an increase in P/B ratio magnitude at the high temperature sampling. The high temperature data set also experienced significant increases in error bar magnitude as well as an increase in the slope of the linear regression, compared with room temperature data. Manganese experienced the least substantial change in calibration curve characteristics when comparing data from the two sampling temperatures in Figure 4.3.6. The calibration curves have similar slopes and y-axis intercepts, but the overall linear regression fit has been shifted down due to the lower P/B ratio magnitudes obtained at the

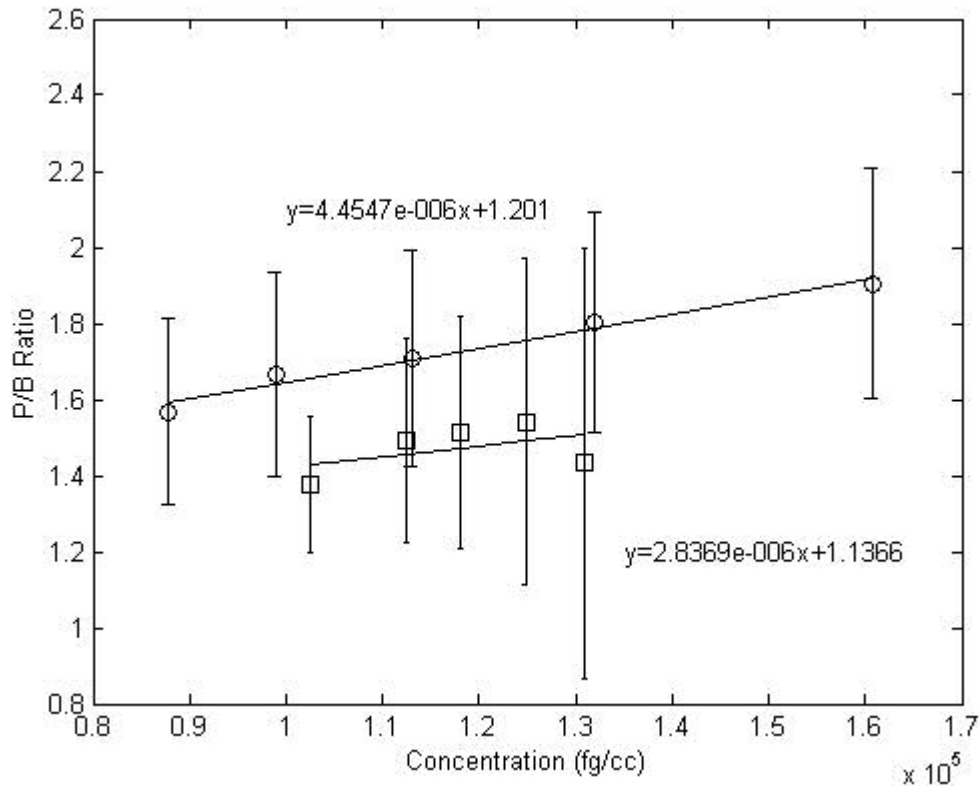


Figure 4.3.6 - P/B ratio as a function of Mn polydisperse aerosol concentration taken at room temperature (circles) and 420°C (squares).

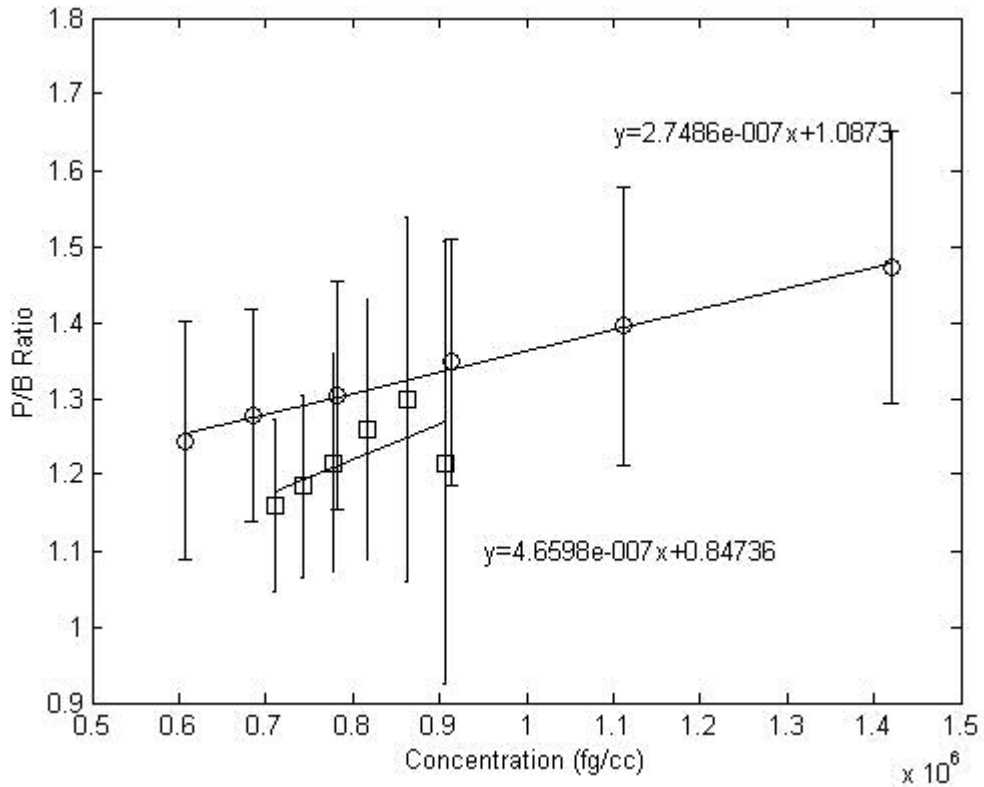


Figure 4.3.7 - P/B ratio as a function of Ti polydisperse aerosol concentration taken at room temperature (circles) and 420°C (squares).

higher sampling temperature. Titanium also experienced little variation in regression fit line slope and y-axis intercept when sampled in the high temperature environment. Figure 4.3.7 shows that the standard deviation of Ti at room temperature was consistent across the concentrations injected while at 420°C the standard deviation was much higher at the higher concentrations.

In summary, there are some general trends that apply to the majority of Figures 4.3.3-4.3.7. The slope of the best fit line for the high temperature was greater than the slope for the room temperature data for all of the elements except Mn, which had very similar trend lines in both data sets. There was more fluctuation in magnitude of the

standard deviation for the high temperature data sets, pointing to less consistent signal detection at a given elemental concentration. The P/B ratio magnitudes decreased during high temperature sampling for every element except Mg, which experienced increased P/B ratios at high temperatures. In all data sets, the P/B ratios decreased with decreasing elemental concentration. Further evidence of this trend can be seen by plotting averaged spectra from each elemental concentration on a graph. An example is shown below in Figure 4.3.8 where Ti spectra sampled at room temperature are plotted. Titanium, Ti (II), spectral emission produces multiple lines that are located at 323, 334, 336, 337, and 338 nm. One challenge arises due to background peaks that are present in the wavelength region where the Ti (II) lines are located; background peaks interfere with the correct quantification of any analyte. Figure 4.3.8 plots spectra averaged over 500 single shots at

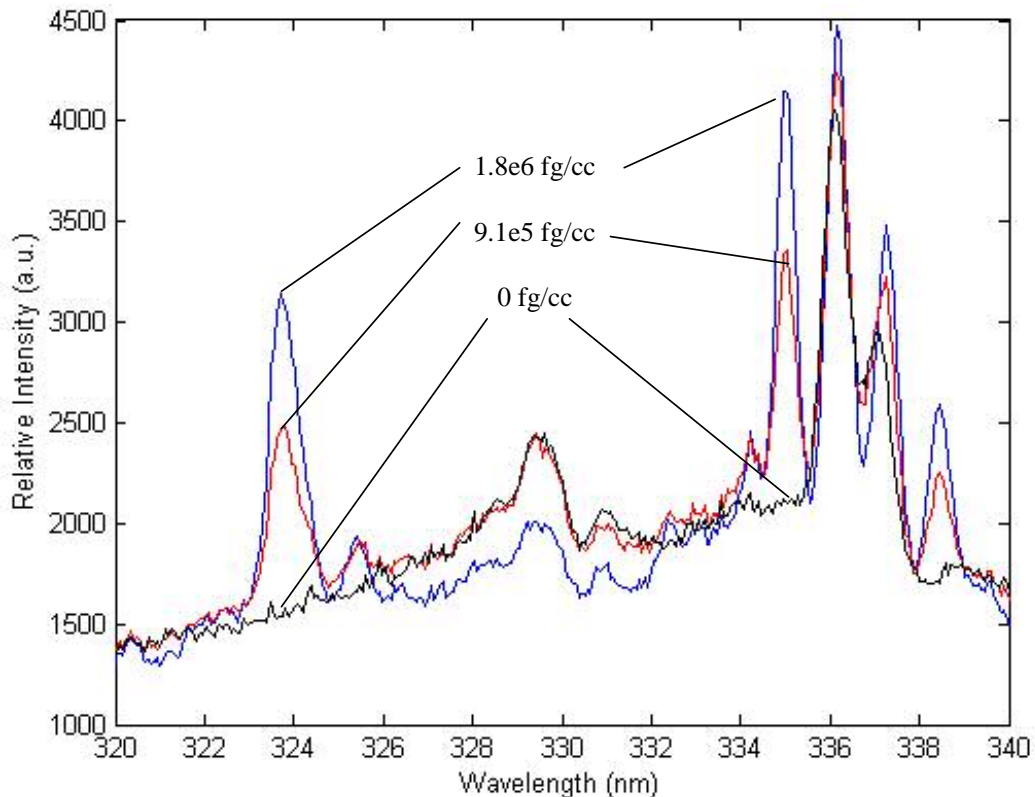


Figure 4.3.8 - Concentration averaged spectra showing Ti elemental peaks sampled at room temperature.

each Ti (II) particulate concentration. Peaks at 323, 334, and 338 nm tend to decrease with decreasing elemental concentration, proving these peaks are related to the analyte. Other peaks, possibly associated with NH or N₂, at 336 and 337 nm do not decrease in magnitude proportionally to the concentration.

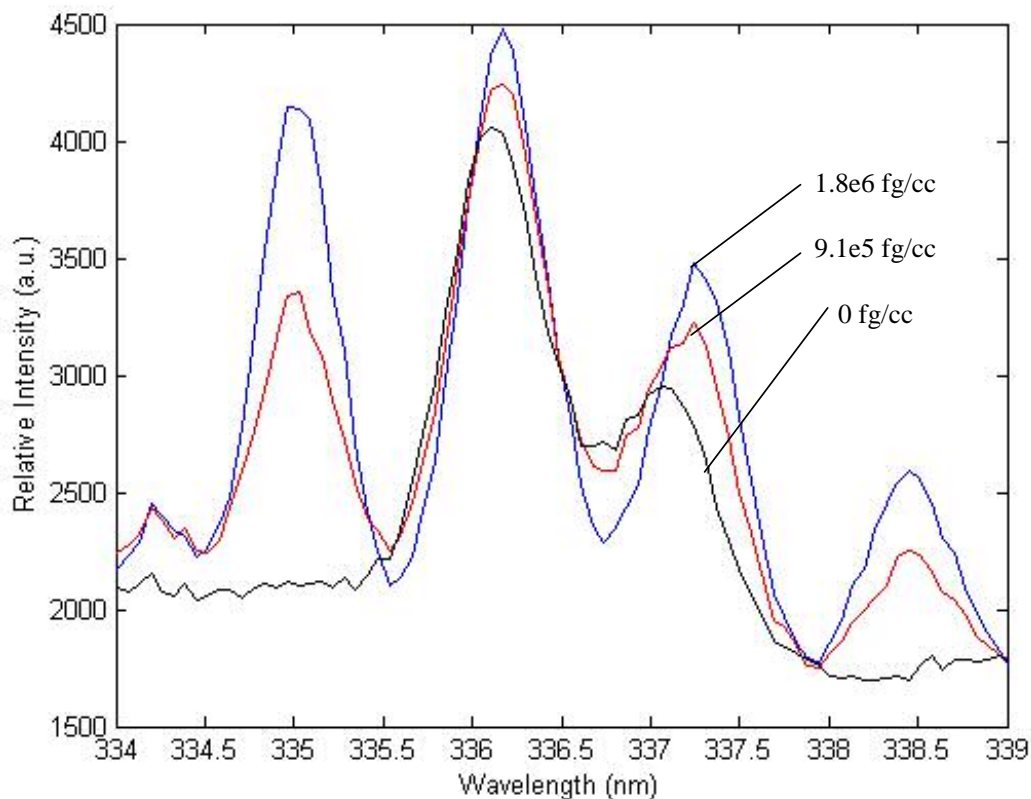


Figure 4.3.9 - Detailed view of 334-339 nm from Ti spectra in Figure 4.3.8.

The Ti peak at 323 nm shows sensitivity to Ti concentration, and the measurement with no aerosol indicates no significant background interfering. In the Ti spectrum in Figure 4.3.9, the four peaks between 335 and 340 nm appear as strong peaks and all are possibly related to the injected element according to the NIST Atomic Database. But the decrease in peak intensity of the outer two peaks with decreasing concentration a relationship with Ti, whereas the inner two peaks at 336 nm and 337 nm

remain consistently strong despite the decrease in Ti concentration. These inner peaks are therefore related to some other element or molecule present in the plasma spark volume not related to Ti, possibly NH or N₂ recombination. For this reason, the Ti II peak at 323 nm was used in the calculation of P/B ratios. Similar studies of peak intensity fluctuation with analyte concentration for Mg, Mn, and Cr were performed to verify suitable peaks for the P/B calculations of Figures 4.3.3-4.3.7.

Spectral plots, while useful for monitoring peak intensity, can also provide information about the background emission during sampling, and variation in the background emission. The base, or background, is the average spectral intensity over a wavelength range and the noise is fluctuation in the signal about the base.

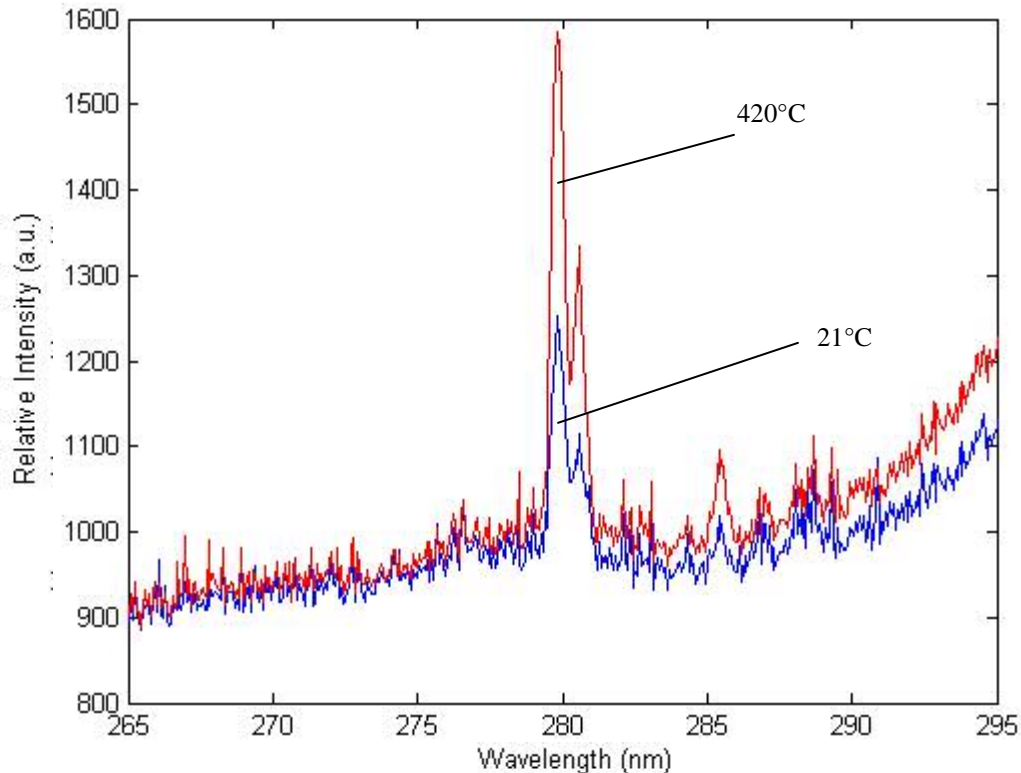


Figure 4.3.10 - Comparison of averaged Mg spectra at room temperature and high temperature with an aerosol concentration of approximately 9500 fg/cc.

The plots in Figures 4.3.3-4.3.7 provide information about the P/B ratio magnitude but plotting the spectra representing the averages of the 500 single shots will enable comparison of the base and peak intensities, rather than just the ratios of those values. Figure 4.3.10 contains spectra obtained by averaging the 500 single shot spectra taken at similar Mg concentrations of approximately 9,500 fg/cc. This allows for direct comparison of the effects of temperature and exhaust species on the Mg spectra. The background and noise signals are almost identical on the left side of the peak while the intensities gradually change and shift apart as the wavelength increases. The Mg peak has a much higher intensity at the elevated temperature and will, therefore, have a higher P/B ratio than the room temperature measurements since base intensity levels are similar.

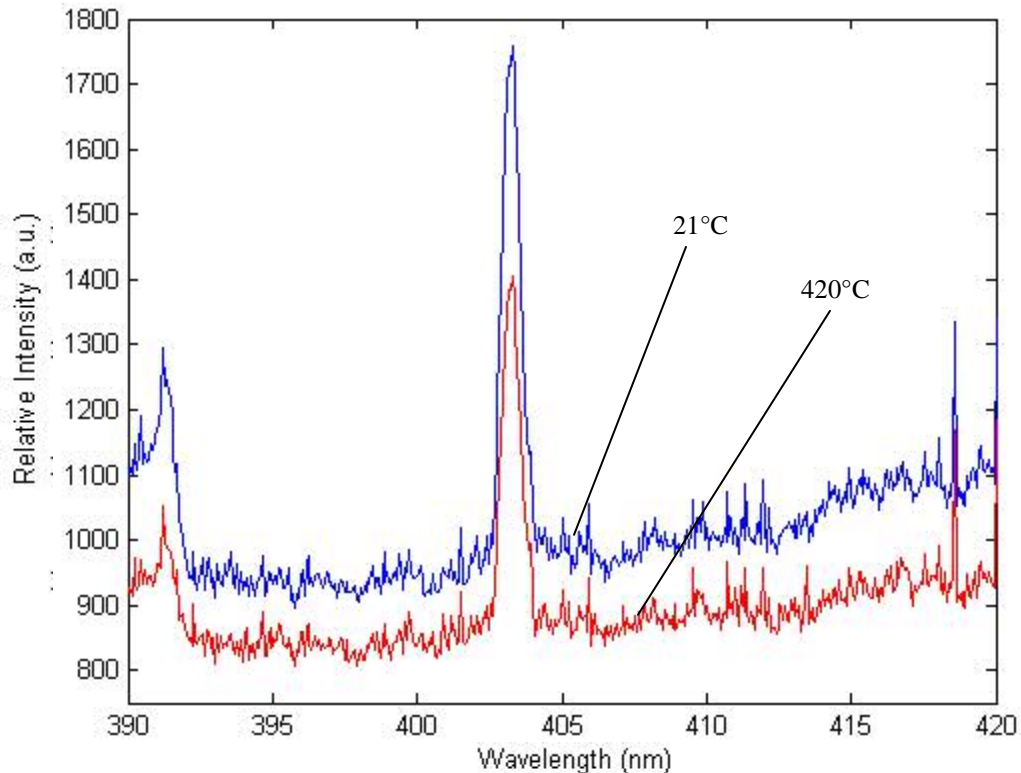


Figure 4.3.11 - Comparison of averaged Mn spectra at room temperature and high temperature with aerosol concentration approximately 113000 fg/cc.

This corresponds to Figure 4.3.5 where the P/B ratio at 9,500 fg/cc is higher for the 420°C data set. Figure 4.3.11 shows the same temperature-based comparison of averaged spectra but for Mn, and the result is quite different. Manganese sampling at an elemental concentration of 113,000 fg/cc showed a drop in both peak and background intensity when flow reactor data at 420°C is compared to room temperature data. Figure 4.3.6 shows that the P/B ratio was higher at room temperature at this elemental concentration.

Matlab was used to calculate the average P/B ratios, to calculate the equation for the line of best fit for the data points, to plot the spectra, and to bin the P/B ratios. The slope from the calibration curve linear regression fit, along with the RMS noise are used in Eq. 4.2 to calculate the LOD concentration for each element.

$$LOD = \frac{3N_{RMS} p}{m\bar{I}} \quad (4.2)$$

$$N_{RMS} = \sqrt{\frac{\sum_{k=1}^p (I_k - \bar{I})^2}{p}} \quad (4.3)$$

where m = slope of the linear regression equation,
 N_{RMS} = RMS noise over base intensity,
 I_k = spectral intensity at k^{th} pixel,
 \bar{I} = average spectral intensity over p pixels, and
 p = number of pixels.

For LOD calculations using the equations above, the RMS noise is calculated using Eq. 4.3 with the intensity from 20 pixels on either side of the elemental peak. The LOD was determined with Eq. 4.2 and the results for both room temperature and heated sampling are shown in Table 4.3.1, below. Multiplying by the approximate sample volume of the

Element	Temperature (°C)	Slope - Line of Best Fit	Average Base Intensity (a.u.)	Average RMS Noise	LOD (fg/cc)	LOD (fg)
Cr	21	4.80E-06	8.30E+02	1.10E+02	5.60E+05	4.09E+02
	420	1.00E-05	8.10E+02	1.00E+02	2.60E+05	1.90E+02
Mg	21	1.50E-05	9.70E+02	5.05E+01	2.10E+05	1.53E+02
	420	1.10E-04	9.90E+02	6.29E+01	3.60E+04	2.63E+01
Mn	21	4.50E-06	9.60E+02	1.40E+02	7.00E+05	5.11E+02
	420	2.80E-06	9.00E+02	1.10E+02	8.90E+05	6.50E+02
Ti	21	2.70E-07	1.70E+03	2.90E+02	1.30E+07	9.49E+03
	420	4.70E-07	1.90E+03	3.30E+02	7.90E+06	5.77E+03

Table 4.3.1 - Polydisperse mass detection limits with relevant data for each element.

plasma spark [24] produces the minimum detectable mass of the metallic element necessary for the LIBS system. Carranza and Hahn [24] calculate plasma volume by statistical, physical, and emission based methods. The plasma volume in this case was determined physically by measuring spark length and using a method of similar triangles from known lens focal length to plasma location. The volume was calculated to be approximately 0.73 mm³ for the laser pulse energy of 60 mJ, which is smaller than the volume reported by Carranza in [24] of 1.44 mm³ for a laser pulse energy of 315 mJ. The LOD data for polydisperse aerosol sampling at room temperature and 420°C is summarized for Cr, Mg, Mn, and Ti in Table 4.3.1.

The strong dependence of the detection limits on the slope is evident from Table 4.3.1. The average base intensity and RMS noise, which are also used in the calculation of LOD remain fairly uniform across the temperature range with respect to element. However, slope varies more significantly based on temperature, up to an order of magnitude for both Cr and Mg.

4.4 Dispersity Comparison

The effect of particle size distribution on LIBS detection limits focused on LIBS sampling of polydisperse and monodisperse aerosol concentrations at room temperature and comparing the calibration curves and limits of detection. Due to the size selection process involving the DMA, undiluted elemental particulate concentrations were much lower for the monodisperse aerosol, compared with the polydisperse aerosol concentrations in Table 4.2.1. For this reason, dilution air flow rates were lowered in an effort to maintain concentrations detectable by LIBS and 1000 spectral shots were taken at each particulate concentration. The concentrations of each element and corresponding DMA voltages and centroid particle diameters are given in Table 3.5.2. The decreases in concentration encountered in monodisperse sampling affected particle hit rate as well

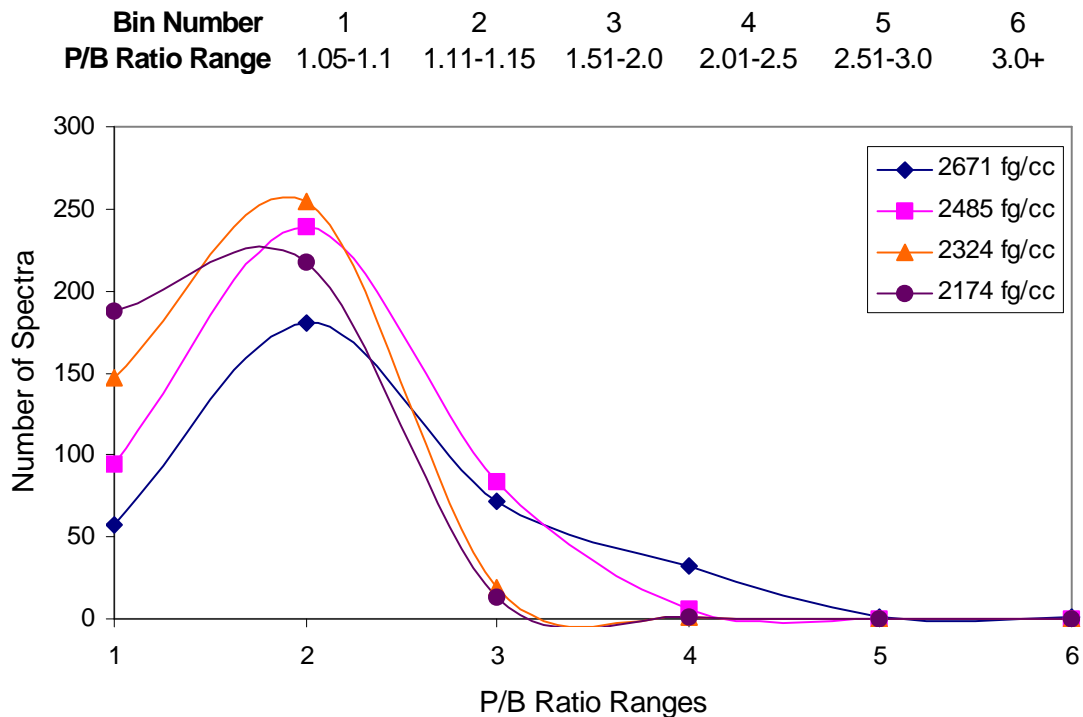


Figure 4.4.1 - Spectral hits binned by P/B ratio magnitude, monodisperse Mg.

as signal intensity. The monodisperse spectral data was processed to monitor the frequency of elemental hits with respect to P/B ratio values. The same criteria for hit acceptance as outlined in Section 4.3 applies to the monodisperse data - 100% of spectra with P/B ratios greater than 1.5 were classified as elemental hits, 97% with S/N ratios between 1.1 and 1.5 were hits, and approximately 85% if S/N ratio was between 1.05-1.1. Similar trends can be seen when comparing the monodisperse Mg data taken at room temperature with the same data taken from polydisperse aerosol sampling. Figure 4.4.1 shows a similar increase in P/B ratio as the concentration increases. Figure 4.4.2 has relatively higher P/B ratios due to the substantially higher elemental concentration in the polydisperse aerosol flow and the presence of larger diameter particles in the plasma volume. Data from both monodisperse and polydisperse test sets are not presented in the

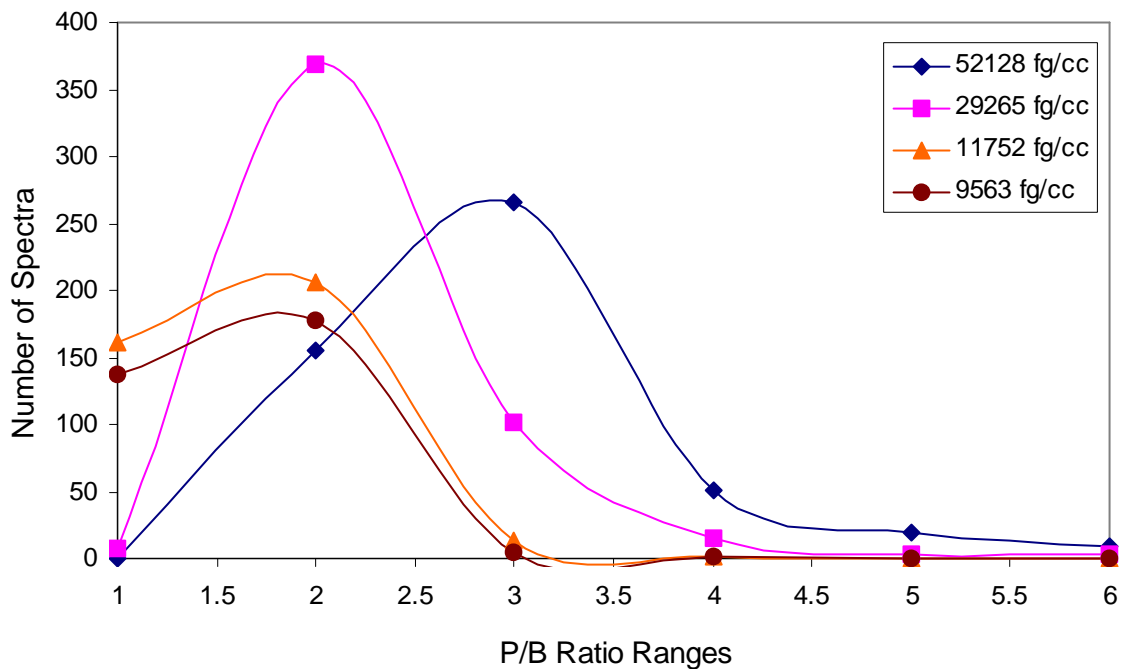


Figure 4.4.2 - Spectral hits binned by P/B ratio magnitude, polydisperse Mg.

same figure due to the differences in concentration. It is important, however, to recognize that the monodisperse aerosol produces similar results of P/B ratio magnitude scaling with concentration.

Figures 4.4.3 and 4.4.4 show the LIBS system calibration curves for Mg monodisperse and polydisperse aerosol flow, respectively. Each point in Figure 4.4.3 represents the average P/B ratio taken from 1000 single shot spectra as a function of

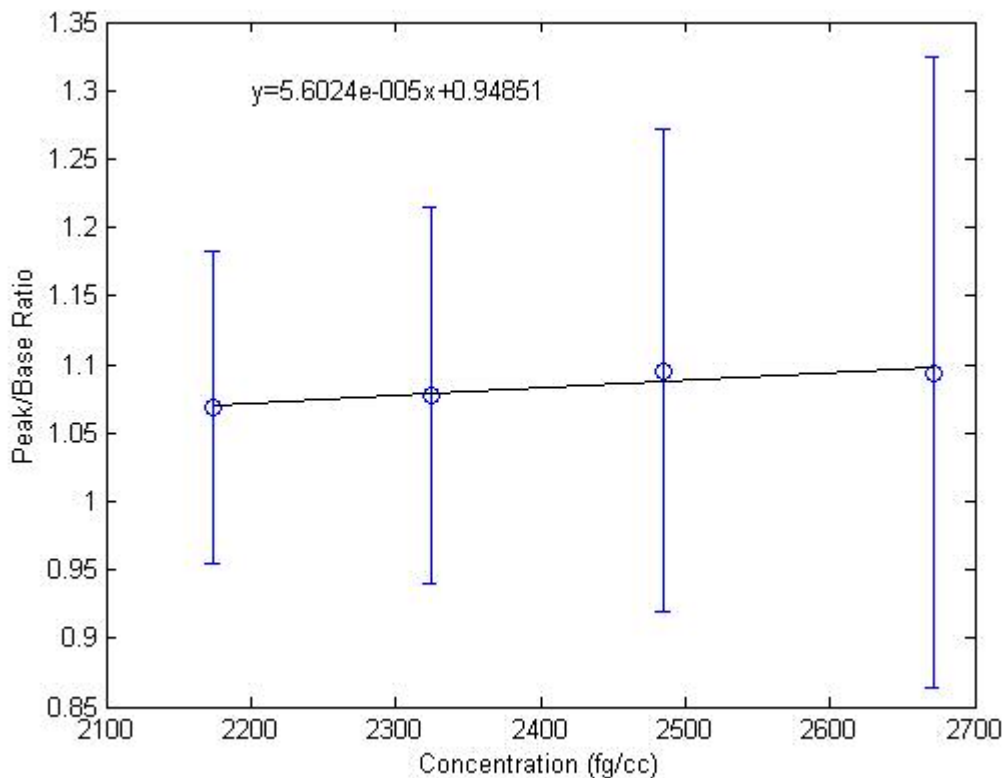


Figure 4.4.3 - P/B ratio as a function of Mg monodisperse aerosol concentration.

monodisperse aerosol concentration. There is very little change in the concentration, and thus minor variation in the P/B ratios. The error bars are +/- 1 standard deviation from the mean, and the magnitudes are large relative to the P/B ratio magnitudes, especially at the higher concentrations. This is due to the large number of spectra that do not contain

elemental peaks. These blank spectra are averaged along with the hits, creating a broader range of P/B ratios. The data points in Figure 4.4.4 represents the average P/B ratio taken from 500 single shot spectra as a function of polydisperse aerosol concentration. Unlike the polydisperse data plots used to determine LOD, the data points in the monodisperse plots are equally spaced due to linear increases in dilution flow rates. The equations in the upper left corners of the plot describe linear regression lines fitted to the data points. Similar calculations were performed to determine calibration curve slopes for the other

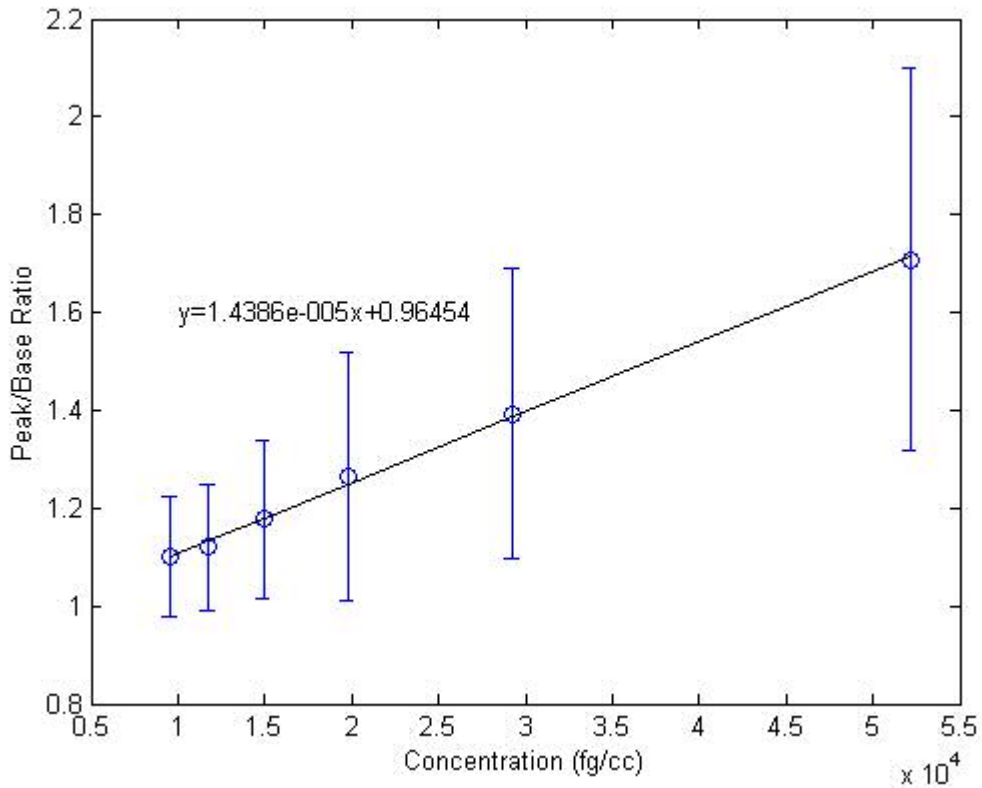


Figure 4.4.4 - P/B ratio as a function of Mg polydisperse aerosol concentration.

three elements and are presented in Table 4.4.1 along with the other variables necessary to calculate the detection limits.

The average P/B ratio points in Figures 4.4.3 and 4.4.4 can also be shown as spectral plots to verify changes in the peak intensity. In Figure 4.4.5, the intensity of the

Mn peak at 403 nm decreases with decreasing aerosol concentration while noise intensity remains unchanged. As a result, the P/B ratio magnitude decreases with decreasing elemental concentration, similar to the results seen in polydisperse testing. The concentrations of the averaged spectra relate to those in Figure 4.4.3. The broad wavelength peaks located on the left of the figure at 390 nm can be attributed to molecular species (primarily CN) present in the spark volume.

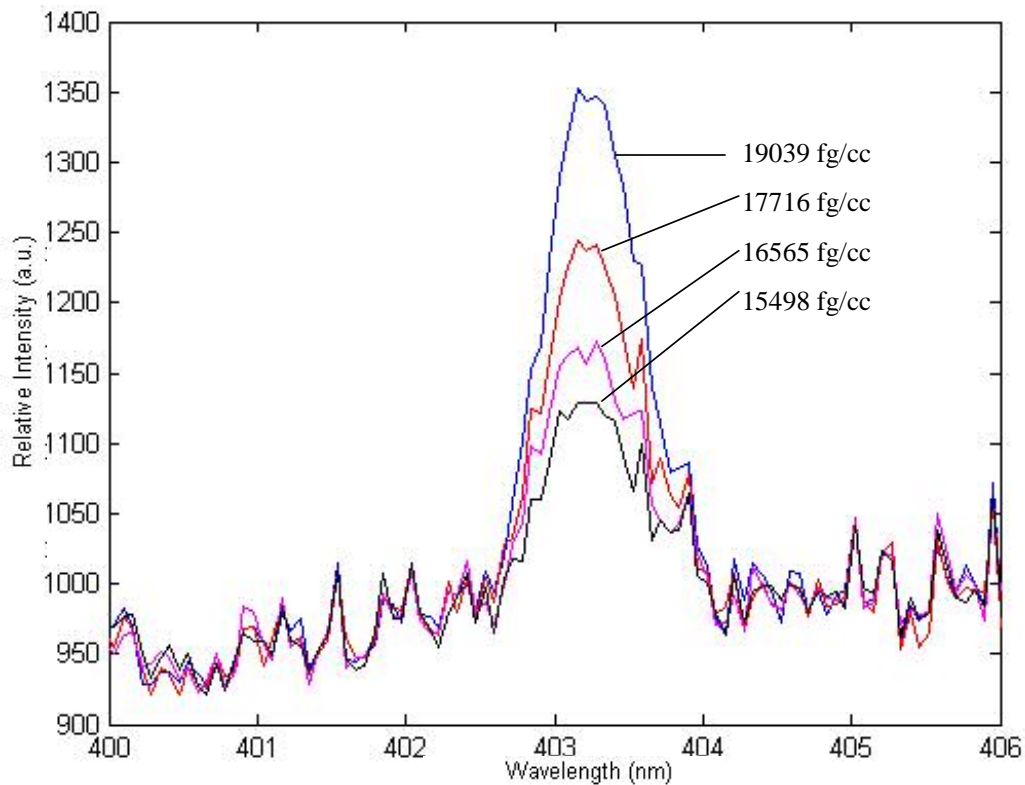


Figure 4.4.5 - Monodisperse concentration averaged spectra showing Mn elemental peaks sampled at room temperature.

Averaged spectra from polydisperse and monodisperse data sets are not plotted on the same graph due to the differences in elemental concentrations. It would not be possible to distinguish the effects of the concentration versus the effects of the dispersity on the spectral intensity. However, the statistical values of average RMS noise and

average baseline intensity along with calibration curve slope can be used to determine detection limits for the elements in monodisperse form. These can then be compared to the LODs calculated from the polydisperse data. The RMS noise is calculated using Eq. 4.3 and the LOD is determined with Eq. 4.2 and the results are shown in Table 4.4.1 along with the room temperature polydisperse results.

Element	Dispersity	Slope - Line of Best Fit	Average Base Intensity (a.u.)	Average RMS Noise	LOD (fg/cc)	LOD (fg)
Cr	Monodisperse	5.57E-05	7.90E+02	3.35E+02	1.60E+05	1.17E+02
	Polydisperse	4.80E-06	8.30E+02	1.10E+02	5.60E+05	4.09E+02
Mg	Monodisperse	5.37E-05	9.05E+02	7.80E+01	1.30E+05	9.49E+01
	Polydisperse	1.50E-05	9.70E+02	5.05E+01	2.10E+05	1.53E+02
Mn	Monodisperse	5.37E-05	7.00E+02	2.60E+02	1.45E+05	1.06E+02
	Polydisperse	4.50E-06	9.60E+02	1.40E+02	7.00E+05	5.11E+02
Ti	Monodisperse	4.70E-06	1.59E+03	4.10E+02	1.15E+06	8.41E+02
	Polydisperse	2.70E-07	1.70E+03	2.90E+02	1.30E+07	9.49E+03

Table 4.4.1 - Monodisperse mass detection limits with relevant data for each element.

By comparing the results in Table 4.4.1, it can be seen that the slope of the calibration curve increased during monodisperse sampling for every element except Mg. The average RMS noise always increased and the average base intensity always decreased for monodisperse data, likely due to the decreased spectral hit rate. These changes led to decreases in detection limits for all four elements during monodisperse sampling. While RMS noise increases, the slope of the linear regression fit increases by a higher relative percentage; thus driving the decreases in detection limits by Eq. 4.2.

4.5 Comparison of Detection Limits

Analysis of the data reveals changes in LIBS sensitivity resulting from ambient temperature differences and aerosol dispersity. Typically, LIBS detection limits

decreased when ambient temperature was raised and when monodisperse particulate aerosol was sampled versus polydisperse aerosol. The mass detection limits are summarized in Table 4.5.1. The detection limit decrease with respect to higher

Element	LOD (fg/cc)		
	Polydisperse 21°C	Polydisperse 420°C	Monodisperse 21°C
Cr	4.09E+02	1.90E+02	1.17E+02
Mg	1.53E+02	2.63E+01	9.49E+01
Mn	5.11E+02	6.50E+02	1.06E+02
Ti	9.49E+03	5.77E+03	8.41E+02

Table 4.5.1 - Mass detection limits for each heavy metal element.

temperature was opposite of what was predicted to occur. The expected result was an increase in LOD due to the change in density, possible chemical quenching effects, and particulate losses to the walls. The higher temperature decreases the density of the carrier flow in which the plasma spark forms. The decrease in air density results in fewer air molecules to be ablated by the laser and thus a smaller plasma spark volume. Therefore, a higher initial concentration of analyte material was expected to be required to achieve detection sensitivity similar to the room temperature data collection. Contrary to expectations, the data shows a slight increase in detectability for Cr, Mg, and Ti with an increase in temperature.

Further comparison between monodisperse and polydisperse data collection at room temperature shows that LOD depended on aerosol dispersity for each of the four elements. Three changes take place when the DMA filters polydisperse aerosol and outputs a monodisperse stream. The slope of the calibration curve increased during monodisperse sampling for every element except Mg and the average RMS noise always increased and the average base intensity always decreased, likely due to the decreased

spectral hit rate. The monodisperse aerosol concentration is significantly lower than the polydisperse concentration and, by definition, monodisperse contains a narrow band of particle diameters as opposed to the full size distribution. The acknowledgement of both changes is important because both impact the change in LOD. All elements tested experienced decreased detection limits by the LIBS setup in the form of monodisperse aerosols. The decrease in elemental concentration resulted in lower P/B ratios, however, LOD is not directly related to P/B ratio magnitude. The root mean square noise and slope of the linear regression fit line influenced the LOD and experienced changes when temperature and dispersity were varied. The slope of the linear regression fit increased during monodisperse testing. This change coincides with the decrease in detection limits, offering an explanation for the occurrence. The polydisperse mass detection limits in Table 4.5.1 represent aerosol sampling in field testing applications where aerosol dispersity can be described with a polydisperse distribution. Monodisperse mass detection limits can be applied to the controlled lab environment. The mass detection limits presented for the LIBS system described here can be compared to those found in literature discussing previous work [14,15,17,35-37].

4.6 Error Analysis

There are many sources of error involved with LIBS spectral analysis due to the physical components in the system. Shot-to-shot variation in the peak signal arises from fluctuations in particulate concentration, particulate size, and laser pulse energy. The fluctuation in the pulse energy alters plasma sampling volume, temperature in the plasma at local thermodynamic equilibrium, and energy transferred to the atoms. These factors

result in statistical variation of the spectral intensity across all wavelengths and thus contribute to altering the detectability limits. Fluctuations in sampling volume alter the probability that particulate will be present in the plasma at a given time. Presently, laser pulse energy cannot be measured while creating a plasma spark and the only method to increase consistency is allowing the laser to run 30-45 minutes before data collection begins. Furthermore, it is unclear how particle location within the plasma affects signal emission collection by the laser focusing lens. The plasma spark emits in every direction, making it reasonable to assume that particle location within the plasma spark can result in solid angles where elemental emission is highest.

CHAPTER 5 Conclusions

5.1 Summary

Laser Induced Breakdown Spectroscopy was studied experimentally to determine the effects of temperature and aerosol dispersity on mass detection limits for Cr, Mg, Mn, and Ti. The tests were performed with a LIBS apparatus designed to perform in situ heavy metal particulate sampling in harsh combustion exhaust environments, specifically applicable to gas turbines. LIBS sampling in polydisperse aerosol streams at 21°C and 420°C and monodisperse aerosol streams at 21°C displayed decisive evidence that ambient temperature and aerosol dispersity affect the mass detection limits achievable by the LIBS system.

Increasing the temperature results in increased LIBS sensitivity (i.e. decreased detection limits). Aerosol dispersity had a similar impact on LIBS detection limits; the detection limits decreased when sampling occurred in monodisperse aerosol compared with polydisperse aerosol. The monodisperse aerosol sampling resulted in higher values for linear regression fit slope and lowered the detection limits of the LIBS system for all four elements tested. The minimum detection limits for the elements during monodisperse sampling at room temperature were found to be 117 fg for Cr, 95 fg for Mg, 106 fg for Mn, and 841 fg for Ti. It was expected that monodisperse and polydisperse aerosol flows would result in similar mass detection limits due to the fact that if 100% of atoms and molecules were ablated in the plasma region, then elemental mass would be the parameter governing P/B ratio and detection limit. The data presented in this thesis suggests that identical mass concentrations in the form of different particle

diameters and particle number densities in the plasma could result in different LIBS detection limits.

5.2 Contributions to LIBS

Articles [1-3,26] were found through a literature review that described experiments in which LIBS was applied in high temperature, combustion environments. Variables influencing the performance of the LIBS technique, such as number of spectra accumulated, detector gate delay, use of background correction [16], electron velocity distributions, degree of ionization, and distribution of excited states [18], have been studied previously. The results presented here provide a first look into quantifying the effects of temperature and aerosol dispersity on LIBS detection capabilities. Understanding how LIBS detection limits are affected by ambient temperature would provide another parameter useful in determining whether LIBS would be an appropriate experimental technique for a specific application.

Monodisperse aerosol flows do not represent aerosol size distributions encountered in emissions monitoring environments. However, the goal of nanoparticle synthesis could include creation of monodisperse particle distributions. LIBS could be useful as a production quality assurance tool measuring synthesized particle diameter through signal emission quantification.

5.3 Future Work

Further study would greatly enhance the quantification of the temperature and aerosol composition effects described above. A set of experiments could be designed to

test a broader range of heavy metal and non-metallic elements. Broad ambient temperature ranges in the sampling region could be used to see how LIBS detection limits change with temperature. The temperature fluctuations could be managed via two methods: with an oven heating the carrier flow and with a combustion reaction. Oven heating provides a method to isolate the effects of temperature on the calibration curves and detection limits. In the case of combustion, the aerosol could be injected into the exhaust or upstream of the combustion reaction. The former combustion technique provides evidence of any post-combustion chemistry or simply how exhaust presence changes LOD, while the latter technique would allow observation of the reaction chemistry effects on the particles.

Similarly, aerosol dispersity could be adjusted by changing the ratio of sheath flow to polydisperse aerosol flow in the DMA, altering the particle mobility bandwidth selected by the instrument. Concentration would change with decreasing mobility bandwidth, but a size distribution approaching monodispersity would result. Testing to determine the effect of particle diameter on signal intensity would also be interesting. Elemental mass concentration could be maintained while changing particle diameter and number density. This would isolate the impact of particle diameter on the LIBS limits of detection.

APPENDIX A Matlab Data Processing Code

A.1 Gate Width/Delay Code

```
clc, clear, close all;
%Calculates peak/base ratio for Chromium as a function of gate width and delay

%Opens single shot spectra of background noise to label x-axis with wavelength
x=[4 8 12 16 20 24];
x2=[12 18 24 30 36];

%Files from laser power at 30 mJ
%Opens spectra in file at 15 microsecond width
for q=1:6 %actual files 13:18
    for r=1:100
        cr_spectra15(:,q,r)=dlmread(['FILENAME',num2str(q+12),'_num2str(r)'.txt'],' ', 0, 2);
        noise_avg15(q,r)=mean(cr_spectra15(591:630,q,r)).*53;
        peak_int15(q,r)=sum(cr_spectra15(631:683,q,r));
        pb_ratio15(q,r)=peak_int15(q,r)/noise_avg15(q,r);
    end
    avg_pb_ratio15(q)=mean(pb_ratio15(q,:));
    stan_dev15(q)=std(pb_ratio15(q,:));
end
ratio15=avg_pb_ratio15(1:6);
std15=stan_dev15(1:6);

%Opens spectra in file at 20 microsecond width
for s=1:6 %actual files 19:24
    for t=1:100
        cr_spectra20(:,s,t)=dlmread(['FILENAME',num2str(s+18),'_num2str(t)'.txt'],' ', 0, 2);
        noise_avg20(s,t)=mean(cr_spectra20(591:630,s,t)).*53;
        peak_int20(s,t)=sum(cr_spectra20(631:683,s,t));
        pb_ratio20(s,t)=peak_int20(s,t)/noise_avg20(s,t);
    end
    avg_pb_ratio20(s)=mean(pb_ratio20(s,:));
    stan_dev20(s)=std(pb_ratio20(s,:));
end
ratio20=avg_pb_ratio20(1:6);
std20=stan_dev20(1:6);

%Files from laser power at 60 mJ
%Opens spectra in file at 15 microsecond width
for i=1:5 %actual files 25:30
    for j=1:100
        cr_spectra_15(:,i,j)=dlmread(['FILENAME',num2str(i+24),'_num2str(j)'.txt'],' ', 0, 2);
        noise_avg_15(i,j)=mean(cr_spectra_15(591:630,i,j)).*53;
        peak_int_15(i,j)=sum(cr_spectra_15(631:683,i,j));
        pb_ratio_15(i,j)=peak_int_15(i,j)/noise_avg_15(i,j);
    end
    avg_pb_ratio_15(i)=mean(pb_ratio_15(i,:));
    stan_dev_15(i)=std(pb_ratio_15(i,:));
end
ratio_15=avg_pb_ratio_15(1:5);
std_15=stan_dev_15(1:5);
```

```

%Opens spectra in file at 30 microsecond width
for s=1:5 %actual files 43:48
    for t=1:100
        cr_spectra30(:,s,t)=dlmread(['FILENAME',num2str(s+42),'_num2str(t)'.txt'],' ', 0, 2);
        noise_avg30(s,t)=mean(cr_spectra30(591:630,s,t)).*53;
        peak_int30(s,t)=sum(cr_spectra30(631:683,s,t));
        pb_ratio30(s,t)=peak_int30(s,t)/noise_avg30(s,t);
    end
    avg_pb_ratio30(s)=mean(pb_ratio30(s,:));
    stan_dev30(s)=std(pb_ratio30(s,:));
end
ratio30=avg_pb_ratio30(1:5);
std30=stan_dev30(1:5);

%Plotting of the peak/base ratios as a function of gate delay and varying the gate width
subplot(2,2,1), plot(x,ratio15,'ko')
errorbar(x,ratio15,std15,'ko')
text(15,1.4,'15 \mus, 30 mJ')
ylabel('P/B Ratio')
subplot(2,2,2), plot(x,ratio20,'ks')
errorbar(x,ratio20,std20,'ks')
text(15,1.5,'20 \mus, 30 mJ')
subplot(2,2,3), plot(x2,ratio_15,'kd')
errorbar(x2,ratio_15,std_15,'kd')
text(25,1.5,'15 \mus, 60 mJ')
xlabel('Gate Delay (\mus)')
ylabel('P/B Ratio')
subplot(2,2,4), plot(x2,ratio30,'kv')
errorbar(x2,ratio30,std30,'kv')
text(25,1.5,'30 \mus, 60 mJ')
xlabel('Gate Delay (\mus)')

figure;
plot(x,ratio15,'ko-', 'linewidth',2); hold on;
plot(x,ratio20,'ks:', 'linewidth',2);hold on;
plot(x2,ratio_15,'kd-', 'linewidth',2); hold on;
plot(x2,ratio30,'kv--', 'linewidth',2)
legend('15 \mus, 30 mJ','20 \mus, 30 mJ','15 \mus, 60 mJ','30 \mus. 60 mJ',2)
ylabel('P/B Ratio')
xlabel('Gate Delay (\mus)')

ratio15
std15
ratio20
std20
ratio_15
std_15
ratio30
std30

disp('Done')

```

A.2 Limit of Detection Calculation - LOD, Average Spectrum, and Spectral Hits Plotting

```

clc, clear, close all;

%Calculates and plots concentration vs. spectral intensity
%Laser power at 60 mJ

%Opens single shot spectra of background noise to label x-axis with wavelength
x=[233770 183040 150400 128800 112630 100050];
x2orig=[24870 23690 22430 21360 20390 19490];
x2=x2orig.*6;
lambda=dlmread(['FILENAME'],' ', [0 0 1023 0]);
lambda2=dlmread(['FILENAME'],' ', [0 0 1023 0]);
m=[1 1 1 1 1 1];
n=[0 0 0 0 0 0];
mm=[1 1 1 1 1 1];
nn=[0 0 0 0 0 0];

%Opens spectra in file and calculates peak/base ratios and averages spectra over analyte concentration for COLD.
for i=1:6
    for j=1:500

spectra(:,i,j)=dlmread(['C:\Kratzsch\Research\Data\081104_polycold\Cr_text\Run',num2str(i),'_'num2str(j),
'.txt'],' ', 0, 2);
        peak_area(i,j)=sum(spectra(635:641,i,j));
        baseline(i,j)=(sum(spectra(611:630,i,j))+sum(spectra(690:709,i,j)))/40;
        base_area(i,j)=baseline(i,j).*7;
        for p=1:20 %RMS noise calculation, pixels 479-498
            noiserms(p,i,j)=spectra(p+610,i,j)-baseline(i,j);
            noiserms_sq(p,i,j)=noiserms(p,i,j)^2;
        end
        sum_noiserms_sq(i,j)=sum(noiserms_sq(:,i,j));
        N_rms(i,j)=(sum_noiserms_sq(i,j)/20)^0.5;
        pbLOD(i,j)=peak_area(i,j)/base_area(i,j);
        if peak_area(i,j)>=(N_rms(i,j)+baseline(i,j))*7 % 1.15*base_area(i,j) %Determines whether or not
there is a spectral hit and calculates p/b ratio
            PBratio(i,j)=peak_area(i,j)/base_area(i,j);
            m(i)=m(i)+1;
            n(i)=n(i)+1;
            hit(:,i,n(i))=spectra(:,i,j);
        end
        avghit=mean(hit,3);
    end

%Peak/base ratio of every spectral shot for LOD plot
    avg_pbLOD(i)=mean(pbLOD(i,:));
    std_pbLOD(i)=std(pbLOD(i,:));
    avgN_rms(i)=mean(N_rms(i,:));
    avg_baseline(i)=mean(baseline(i,:));

    avg_N_rms(i)=mean(N_rms(i,:));
    std_N_rms(i)=std(N_rms(i,:));
    relstd_N_rms(i)=std_N_rms(i)/avg_N_rms(i);

```

```

%Average peak/base ratio based on spectral hits only
avg_spectra=mean(spectra,3);
avg_pb_ratio(i)=mean(PBratio(i,:));
stan_dev_pb(i)=std(PBratio(i,:));
disp(['Number of Spectra Taken=',num2str(j)]);
disp(['Number of Hits=',num2str(m-1)]);
hit_ratio=((m-1)/j)*100;
disp(['Hit Percentage=',num2str(hit_ratio),'%']);
end

totalavgN_rms=mean(avgN_rms(:));
totalavgbaseline=mean(baseline(i,:));
totalavgN_rmsFR=mean(avgN_rmsFR(:));
totalavgbaselineFR=mean(baselineFR(q,:));

avgrelstd_N_rms=mean(relstd_N_rms(:));
avgrelstd_N_rmsFR=mean(relstd_N_rmsFR(:));

%Calculates linear regression fit for LOD peak/base ratio data and creates plot COLD
fitcoeff=polyfit(x,avg_pbLOD,1);
fitline=polyval(fitcoeff,x);
figure;
plot(x,avg_pbLOD,'ko'); hold on;
errorbar(x,avg_pbLOD,std_pbLOD,'bo');
plot(x,fitline, 'k-');
ylabel('P/B Ratio')
xlabel('Concentration (fg/cc)')
text(100000,2.2,['y=',num2str(fitcoeff(1)),'x+',num2str(fitcoeff(2))])
%Calculates linear regression fit for LOD peak/base ratio data and creates plot for HOT FR
fitcoeff=polyfit(x2,avg_pbLODFR,1);
fitline=polyval(fitcoeff,x2);
figure;
plot(x2,avg_pbLODFR,'ko'); hold on;
errorbar(x2,avg_pbLODFR,std_pbLODFR,'bo');
plot(x2,fitline, 'k-');
ylabel('P/B Ratio')
xlabel('Concentration (fg/cc)')
text(120000,2.0,['y=',num2str(fitcoeff(1)),'x+',num2str(fitcoeff(2))])

%Plot of the concentration-averaged spectra
figure
hold on
plot(lambda,avg_spectra(:,1),'b'); hold on;
plot(lambda,avg_spectra(:,3),'r'); hold on;
plot(lambda,avg_spectra(:,5),'k');
% C=['b','r','m','k'];
% for k=1:4
% plot(lambda,avg_spectra(:,k),C(k));
% end
% axis([260 300 800 3000])
xlabel('Wavelength (nm)')
ylabel('Relative Intensity (a.u.)')

%Plot of the concentration-averaged spectra of HITS ONLY
figure

```

```

hold on
plot(lambda,avghit(:,1),'b'); hold on;
plot(lambda,avghit(:,3),'r'); hold on;
plot(lambda,avghit(:,5),'k');
% C=['b','r','m','k'];
% for k=1:4
%   plot(lambda,avghit(:,k),C(k));
% end
%axis([260 300 500 3000])
xlabel('Wavelength (nm)')
ylabel('Relative Intensity (a.u.)')

%LOD calculation
old_LOD=(2*avgrestd_N_rms)/fitcoeff(1);
old_LODFR=(2*avgrestd_N_rmsFR)/fitcoeff2(1);
LOD=(3*totalavgN_rms*7)/(fitcoeff(1)*totalavgbaseline);
LODFR=(3*totalavgN_rmsFR*7)/(fitcoeff2(1)*totalavgbaselineFR);

%Output data
avg_pbLOD
std_pbLOD
avg_pbLODFR
std_pbLODFR
totalavgN_rms
totalavgbaseline
totalavgN_rmsFR
totalavgbaselineFR
disp(['slope=',num2str(fitcoeff(1))]);
disp(['y-intercept=',num2str(fitcoeff(2))]);
disp(['LOD=',num2str(LOD,3),' fg/cc']);
disp(['slopeFR=',num2str(fitcoeff2(1))]);
disp(['y-interceptFR=',num2str(fitcoeff2(2))]);
disp(['LODFR=',num2str(LODFR,3),' fg/cc']);
old_LOD
old_LODFR

disp('Done')

```


A.3 Peak-to-Base Ratio Calculation and Binning

clc, clear, close all;

```
%Opens single shot spectra of background noise to label x-axis with wavelength
lambda=dlmread(['C:\Kratzsch\Research\Data\081104_polycold\Mn_text\Run1_1.txt'],'', [0 0 1023 0]);
%lambda=dlmread(['C:\Kratzsch\Research\Data\081104_polyhot\Mn_text\Run1_1.txt'],'', [0 0 1023 0]);
x=[1 1.5 2 2.5 3 3.5 4];
a=[0 0 0 0 0 0];
b=[0 0 0 0 0 0];
c=[0 0 0 0 0 0];
d=[0 0 0 0 0 0];
e=[0 0 0 0 0 0];
f=[0 0 0 0 0 0];
g=[0 0 0 0 0 0];
h=[0 0 0 0 0 0];

%Opens spectra in file and calculates peak/base ratios and averages spectra over analyte concentration.
for i=1:7
    for j=1:500
        spectra(:,i,j)=dlmread([FILENAME'_num2str(j)'.txt'],'', 0, 2);
        %spectra(:,i,j)=dlmread([FILENAME'_num2str(j)'.txt'],'', 0, 2);
        peak_area(i,j)=sum(spectra(512:522,i,j));
        baseline(i,j)=(sum(spectra(481:500,i,j))+sum(spectra(528:547,i,j)))/40;
        base_area(i,j)=baseline(i,j).*11;
        if peak_area(i,j)>4*base_area(i,j) %Determines whether or not there is a spectral hit and calculates p/b
ratio
            a(i)=a(i)+1;
        end
        if peak_area(i,j)>3.5*base_area(i,j) %Determines whether or not there is a spectral hit and calculates
p/b ratio
            b(i)=b(i)+1;
        end
        if peak_area(i,j)>3*base_area(i,j) %Determines whether or not there is a spectral hit and calculates p/b
ratio
            c(i)=c(i)+1;
        end
        if peak_area(i,j)>2.5*base_area(i,j) %Determines whether or not there is a spectral hit and calculates
p/b ratio
            d(i)=d(i)+1;
        end
        if peak_area(i,j)>2*base_area(i,j) %Determines whether or not there is a spectral hit and calculates p/b
ratio
            e(i)=e(i)+1;
        end
        if peak_area(i,j)>1.5*base_area(i,j) %Determines whether or not there is a spectral hit and calculates
p/b ratio
            f(i)=f(i)+1;
        end
        if peak_area(i,j)>1.1*base_area(i,j) %Determines whether or not there is a spectral hit and calculates
p/b ratio
            g(i)=g(i)+1;
        end
        if peak_area(i,j)>1.05*base_area(i,j) %Determines whether or not there is a spectral hit and calculates
p/b ratio
            h(i)=h(i)+1;
        end
    end
end
```

```

        end
    end
end

disp(['P/B>4.0= ',num2str(a)]);
disp(['P/B>3.5= ',num2str(b)]);
disp(['P/B>3.0= ',num2str(c)]);
disp(['P/B>2.5= ',num2str(d)]);
disp(['P/B>2.0= ',num2str(e)]);
disp(['P/B>1.5= ',num2str(f)]);
disp(['P/B>1.1= ',num2str(g)]);
disp(['P/B>1.05= ',num2str(h)]);

disp([' P/B>4.0= ',num2str(a)]);
disp(['4.0>P/B>3.5= ',num2str(b-a)]);
disp(['3.5>P/B>3.0= ',num2str(c-b)]);
disp(['3.0>P/B>2.5= ',num2str(d-c)]);
disp(['2.5>P/B>2.0= ',num2str(e-d)]);
disp(['2.0>P/B>1.5= ',num2str(f-e)]);
disp(['1.5>P/B>1.1= ',num2str(g-f)]);
disp(['1.1>P/B>1.05= ',num2str(h-g)]);

disp('Done')

```

Comments: The remainder of Matlab processing code that aided in data conditioning involved modifications of the three main codes presented here.

Bibliography

- [1] Blevins, L.G., Shaddix, C.R., Sickafoose, S.M., Walsh, P.M., "Laser-induced breakdown spectroscopy at high temperatures in industrial boilers and furnaces," *Applied Optics*, V. 42, N. 30, 2003, pp. 6107-6118.
- [2] Neuhauser, R.E., Panne, U., Niessner, R., Wilbring, P., "On-line monitoring of chromium aerosols in industrial exhaust streams by laser-induced plasma spectroscopy (LIPS)," *Fresenius' Journal Analytical Chemistry*, V. 364, 1999, pp. 720-726.
- [3] Buckley, S.G., Johnsen, H.A., Hencken, K.R., Hahn, D.W., "Implementation of laser-induced breakdown spectroscopy as a continuous emissions monitor for toxic metals," *Waste Management*, V. 20, 2000, pp. 455-462.
- [4] Radziemski, L.J., "Review of Selected Analytical Applications of Laser Plasmas and Laser Ablation, 1987-1994," *Microchemical Journal*, V. 50, 1994, pp. 218-234.
- [5] Kurz, R., Brun, K., "Degradation in Gas Turbine Systems," *Journal of Engineering for Gas Turbines and Power*, V. 123, N. 1, 2001, pp. 70-77.
- [6] Wood, M.I., "Gas turbine hot section components: The challenge of 'residual life' assessment," *Proceedings of the Institution of Mechanical Engineers, Part A: Journal of Power and Energy*, V. 214, N. 3, 2000, pp. 193-201.
- [7] Bamberger, E.N., Zaretsky, E.V., Signer, H., "Endurance and Failure Characteristic of Main-Shaft Jet Engine Mearing at 3×10^6 DN", *Journal of Lubrication Technology*, V. 98, N. 4, 1976, pp. 580.
- [8] Ioannides, E., Harris, T.A., Ragen, M., "Endurance of Aircraft Gas Turbine Mainshaft Ball Bearings-Analysis Using Improved Fatigue Life Theory: Part 1 - Application to a Long-Life Bearing," *Journal of Tribology*, V. 112, 1990, pp. 304.
- [9] Harris, T.A., Ragen, M.A., Spitzer, R.F., "The Effect of Hoop and Material Residual Stresses on the Fatigue of High Speed, Rolling Bearings," *Tribology Transactions*, V. 35, 1992, pp. 194-198.
- [10] Averbach, B.L., Bamberger, E.N., "Analysis of Bearing Incidents in Aircraft Gas Turbine Mainshaft Bearings," *Tribology Transactions*, V. 34, 1991, pp. 241-247.
- [11] Fassel, V.A. "Quantitative Elemental Analyses by Plasma Emission Spectroscopy," *Science*, V. 202, 1978, pp. 183-191.
- [12] Nolte, J., *ICP Emission Spectrometry*, Wiley-VCH, Weinheim, 2003, pp.1-43.

- [13] Timmermans, E.A.H., van der Mullen, J.J.A.M., "Microwave Induced Plasma Torches for On-Line Combustion Gas Analysis," *Atomic Spectroscopy*, V. 15, N. 5, 2003, pp. 14-21.
- [14] Hahn, D.W. Flower, W.L., Hencken, K.R., "Discrete Particle Detection and Metal Emissions Monitoring Using Laser-Induced Breakdown Spectroscopy," *Applied Spectroscopy*, V. 51, N. 12, 1997, pp. 1836-1844.
- [15] Fisher, B.T., Johnsen, H.A., Buckley, S.G., Hahn, D.W., "Temporal Gating for the Optimization of Laser-Induced Breakdown Spectroscopy Detection and Analysis of Toxic Metals," *Applied Spectroscopy*, V. 55, No. 10, 2001, pp. 1312-1319.
- [16] Castle, B.C., Talabardon, K., Smith, B.W., Winefordner, J.D., "Variables Influencing the Precision of Laser-Induced Breakdown Spectroscopy Measurements," *Applied Spectroscopy*, V. 52, No. 5, 1998, pp. 649-657.
- [17] Hahn, D.W., Lunden, M.M., "Detection and Analysis of Particles by Laser-Induced Breakdown Spectroscopy," *Aerosol Science and Technology*, V. 33, 2000, pp. 31-48.
- [18] Yalcin, S., Crosley, D.R., Smith, G.P., Faris, G.W., "Influence of Ambient Conditions on the Laser Air Spark," *Applied Physics B*, V. 68, 1999, pp. 121-130.
- [19] Radziemski, L.J., Cremers, D.A., *Laser-Induced Plasmas and Applications*, Marcel Dekker, Inc., New York, 1989, p. 70-72, 110.
- [20] Salzmann, D., *Atomic Physics in Hot Plasmas*, Oxford University Press, New York, 1998, pp. 3, .
- [21] Lee, Y., Song, K., Sneddon, J., *Laser Induced Breakdown Spectroscopy*, Nova Science Publishers, Inc., New York, 2000.
- [22] Lajunen, L.H.J., *Spectrochemical Analysis by Atomic Absorption and Emission*, The Royal Society of Chemistry, Cambridge, 1992, pp. 12-30, 154-203.
- [23] Carranza, J.E., Hahn, D.W., "Sampling Statistics and considerations for single-shot analysis using laser-induced breakdown spectroscopy," *Spectrochimica Acta Part B*, V. 57, 2002, pp. 779-790.
- [24] Carranza, J.E., Hahn, D.W., "Plasma volume considerations for analysis of gaseous and aerosol samples using laser-induced breakdown spectroscopy," *Journal of Analytical Atomic Spectrometry*, V. 17, 2002, pp. 1534-1539.

- [25] Lee, Won-Bae, Wu, Jianyong, Lee, Yong-Il, Sneddon, Joseph, "Recent Applications of Laser-Induced Breakdown Spectrometry: A Review of Material Approaches," *Applied Spectroscopy Reviews*, V. 39, No. 1, 2004, pp. 27-97.
- [26] Rai, V.N., Singh, J.P., Winstead, C., Yueh, F.Y., Cook, R.L., "Laser-Induced Breakdown Spectroscopy of Hydrocarbon Flame and Rocket Engine Simulator Plume," *AIAA Journal*, V. 41, N. 11, 2003, pp. 2192-2199.
- [27] Petzold, A., Schroder, F.P., "Jet Engine Exhaust Aerosol Characterization," *Aerosol Science and Technology*, V. 28, 1998, pp. 62-76.
- [28] Ottesen, D.K., Baxter, L.L., "Laser Spark Emission Spectroscopy for in Situ, Real-Time Monitoring of Pulverized Coal Particle Composition," *Energy and Fuels*, V. 5, 1991, pp. 304-312.
- [29] Johnson, J.J., Hilton, M., Burrows, R., Madden, P., "Characterisation of Particulates emitted from Gas Turbine Exhausts," *Journal Aerosol Science*, V. 31, Suppl. 1, 2000, pp. S618-S619.
- [30] Heland, J., Schafer, K, et. al., "Nonintrusive optical measurements of aircraft engine exhaust emissions and comparison with standard intrusive techniques," *Applied Optics*, V. 39, N. 3, 2000, pp. 441-455.
- [31] Boyle, K.A., "Evaluating Particulate Emissions from Jet Engines: Analysis of Chemical and Physical Characteristics and Potential Impacts on Coastal Environments and Human Health," *Transportation Research Record No.1517, Public-Sector Aviation Issues, Graduate Research Award Papers, 1994-1995*, pp. 1-9.
- [32] TSI Instruments, Model 3075/3076 Constant Output Atomizer Instruction Manual, P/N 1933076, Revision 1, November 2003.
- [33] Knutson, E.O., Whitby, K.T., "Aerosol Classification by Electric Mobility: Apparatus, Theory, and Applications," *Journal of Aerosol Science*, V. 6, 1975, pp. 443-451.
- [34] Reist, P.C., *Aerosol Science and Technology*, McGraw-Hill, Inc., New York, 1993, p. 201-207.
- [35] Lithgow, G.A., Robinson, A.L., Buckley, S.G., "Ambient measurements of metal-containing PM_{2.5} in an urban environment using laser-induced breakdown spectroscopy," *Atmospheric Environment*, V. 38, 2004, pp. 3319-3328.
- [36] Mg, K.C., Ayala, J.B., Simeonsson, J.B., Winefordner, J.D., "Laser-Induced Plasma Atomic Emission Spectrometry in Liquid Aerosols," *Analytica Chimica Acta*, V. 269, 1992, pp. 123-128.

- [37] Panne, U., Neuhauser, R.E., Theisen, M., Fink, H., Niessner, R., "Analysis of Heavy Metal Aerosols on Filters by Laser-Induced Plasma Spectroscopy," *Spectrochimica Acta, Part B*, V. 56, 2001, pp. 839-850.

References not directly quoted:

Manning, T.J., Grow, W.R., "Inductively Coupled Plasma - Atomic Emission Spectrometry," *The Chemical Educator*, V. 2, N. 1, 1997, pp. 1-19.

TSI Instruments, Model 3025A Ultrafine Condensation Particle Counter, Product Information.

Johnson, M.P., Hilton, M., Waterman, D.R., Black, J.D., "Development of techniques to characterize particulates emitted from gas turbine exhausts," *Measurement Science and Technology*, V. 14, 2003, pp. 1146-1150.

Rusak, D.A, Castle, B.C., Smith, B.W., Wineforder, J.D., "Recent trends and the future of laser-induced plasma spectroscopy," *Trends in Analytical Chemistry*, V. 17, N. 8&9, 1998, pp. 453-461.